The introduction of Observation-Based Physics into the WAM Wave Model and Wave-Coupled Interactions

Joshua S. Kousal

https://orcid.org/0000-0002-5134-5653

A thesis submitted in total fulfilment for the Doctor of Philosophy (Ph.D.) degree

November, 2022

THE UNIVERSITY OF MELBOURNE, AUSTRALIA

UNIVERSITY OF HAMBURG, GERMANY

This page intentionally left blank.

Supervisors

Prof. Alexander Babanin

Prof. Corinna Schrum

Dr. Joanna Staneva

Dr. Jean Bidlot

Prof. Ian Young

Date of Disputation

June 7th, 2024

This page intentionally left blank.

Abstract

Ocean surface waves are an unparalleled ocean phenomenon, wreaking havoc on ocean-going vessels and spreading their tendrils into effects on many aspects of weather and climate. To understand and predict these waves, the best tool available is the third-generation spectral wave model. These models predict the growth, decay, and transformation of wind-generated waves. The modern wave physics package for such models is the observation-based approach developed by A. V. Babanin, I. R. Young, M. A. Donelan, M. L. Banner and W. E. Rogers (hereafter BYDBR). Its source functions were measured and therefore are not subject to tuning (within confidence limits of the measurements). Furthermore, the observations revealed and/or quantified physical phenomena missing or neglected in other source-term packages for spectral wave models such as non-linear airflow separation (hence relative reduction of wind input at strong winds), steepness-dependent wave growth (making the wind input a weakly non-linear function of the wave spectrum), negative wind input under adverse winds, two-part wave dissipation consisting of a local in wavenumber space term and a cumulative term (which is an integral of the spectrum), a wave breaking threshold below which no breaking occurs, and swell decay due to interaction with and production of oceanic turbulence. This observation-based physics is available in two of the three dominant third-generation spectral wave models, WAVEWATCH-III and SWAN, but not yet WAM, the introduction of which (coding, testing and validation for both the ECMWF- and Hereon-managed versions of WAM) is a key outcome of this thesis, and enables its use by the remaining third of the research and practical oceanographic community.

This observation-based physics is primarily concerned with the open ocean however, and neglects regions which are dominated by different physical processes, such as the polar regions. These regions are amongst those changing most rapidly in response to climate change, and contribute the large uncertainty as to how the climate will continue to evolve over the next century. In these regions - or more specifically, what's known as the Marginal Ice Zone - waves and sea ice form a closely coupled system: waves govern sea ice through stress, floe break-up and wave-induced currents, whilst sea ice affects waves through attenuation and reflection. The break-up of sea ice by waves is particularly important as it can regulate air-sea interaction and consequently also regulate the growth and melt of sea ice. This coupled nature between waves and sea ice is complex and generally neglected in modelling of the polar climate system (especially at the large scale). Here we extend the observation-based physics approach to the Marginal Ice Zone to formulate a new model

for wave-sea ice interactions. Our approach builds upon previous investigations of wave-sea ice interaction and can be summarised as follows: 1) sea ice takes a binary form, either 'broken' or 'unbroken', 2) waves may break sea ice, transitioning it from unbroken to broken, 3) a threshold separating breaking and non-breaking wave fields is used to identify when this occurs, 4) two modes of attenuation for waves in ice (dependent upon the ice state), representing the observed on/off switch in wave attenuation. By characterising wave attenuation and sea ice break-up as described above, we achieve a two-way wave-sea ice coupling, thereby allowing wave-sea ice feedbacks. This model is then applied to an Antarctic case study for summer of 2019/2020. We demonstrate that our model can very accurately simulate both the wave field within, and the evolution of, the Marginal Ice Zone. These results further demonstrate the validity of the observation-based approach, as well as substantiate the various observation-based elements drawn on here and their suitability to operate in combination. Furthermore, the results substantiate that waves have a critical influence on the morphology of the Marginal Ice Zone.

As shown above, waves are important not only in their own right, but also because they regulate other domains of the Earth system. The ocean is no exception. Next we consider the effect of waves in the ocean, consistent with the BYDBR observation-based physics: waves, through the process of swell decay, can produce turbulence and mixing deep within the ocean. Ocean models typically neglect this, and we establish here that this is likely a source of considerable bias in such models. This is done through the introduction of this effect into the NEMO ocean model and investigation of its role. We find that this wave-coupled process is a vital source of mixing throughout the upper ocean, and its inclusion can improve oceanic predictions in a physically consistent manner.

Zusammenfassung

Wellen an der Meeresoberfläche sind ein einzigartiges Phänomen des Ozeans mit teils verheerenden Auswirkungen auf Hochseeschiffe, aber auch mit Auswirkungen auf viele Aspekte des Wetters und des Klimas. Das beste verfügbare Instrument zum Verständnis und zur Vorhersage dieser Wellen ist das spektrale Wellenmodell der dritten Generation. Diese Modelle prognostizieren das Wachstum, den Zerfall und die Umwandlung durch Wind erzeugter Wellen. Das moderne Wellenphysik-Paket für solche Modelle ist der von A. V. Babanin, I. R. Young, M. A. Donelan, M. L. Banner und W. E. Rogers (im Folgenden: BYDBR) entwickelte beobachtungsbasierte Ansatz. Die Quellenfunktionen wurden gemessen und werden daher nicht für das Modelltuning verwendet (lediglich innerhalb der Messunsicherheit). Darüber hinaus wurden durch diese Beobachtungen physikalische Phänomene entdeckt und/oder quantifiziert, die in anderen Quellterm-Paketen für spektrale Wellenmodelle fehlen oder vernachlässigt werden, wie z. B. nichtlineare Luftstromtrennung (ie zu einer relativen Verringerung des Windeintrages bei starkem Wind führt), steilheitsabhängiges Wellenwachstum (wodurch der Wind-input zu einer schwach nichtlinearen Funktion des Wellenspektrums wird), negativer Windeintrag bei ungünstigen Winden, zweiteilige Wellendissipation, bestehend aus einem lokalen Term im Wellenzahlraum und einem kumulativen Term (der ein Integral des Spektrums ist), eine Wellenbrechungsschwelle, unterhalb derer keine Brechung auftritt, und Abklingen der Dünung aufgrund der Wechselwirkung mit und der Erzeugung von ozeanischer Turbulenz. Diese auf Beobachtungen basierende Physik ist in zwei der drei häufig verwendeten spektralen Wellenmodelle der dritten Generation, WAVEWATCH-III und SWAN, verfügbar, aber noch nicht in WAM. Die Implementierung dieser Beobachtungsbasierten Physik (Programmierung, Test und Validierung sowohl für die vom ECMWF als auch für die von Hereon verwaltete Version von WAM) ist ein wesentliches Ergebnis dieser Arbeit ist und seine Nutzung durch das verbleibende Drittel der ozeanographischen Forschung und angewandten Ozeanographie ermöglicht.

Diese beobachtungsbasierte Physik befasst sich jedoch in erster Linie mit dem offenen Ozean und vernachlässigt Regionen, die von anderen physikalischen Prozessen dominiert werden, wie z. B. die Polarregionen. Die Polarregionen gehören zu den Regionen, die sich durch den Klimawandel am schnellsten verändern, und tragen wesentlich zur Unsicherheit bei, wie sich das Klima im nächsten Jahrhundert weiter entwickeln wird. In diesen Regionen - genauer gesagt in der sogenannten Randeiszone - bilden Wellen und Meereis ein eng gekoppeltes System: Wellen beeinflussen das Meereis durch Spannung, Schollenbruch und welleninduzierte Strömungen, während das Meereis

die Wellen durch Dämpfung und Reflexion beeinflusst. Das Aufbrechen von Meereis durch Wellen ist besonders wichtig, da es die Wechselwirkung zwischen Luft und Meer und damit auch das Wachstum und Schmelzen des Meereises regulieren kann. Diese Kopplung zwischen Wellen und Meereis ist komplex und wird in der Regel bei der Modellierung des polaren Klimasystems (insbesondere auf großenn Skalen) vernachlässigt. In dieser Arbeit erweitern wir den auf Beobachtungen basierenden physikalischen Ansatz auf die Randeiszone und formulieren ein neues Modell für die Wechselwirkungen zwischen Wellen und Meereis. Unser Ansatz baut auf früheren Untersuchungen der Wechselwirkung zwischen Wellen und Meereis auf und lässt sich wie folgt zusammenfassen: 1) Meereis nimmt eine binäre Form an, entweder "gebrochen" oder "ungebrochen", 2) Wellen können Meereis brechen, wodurch es von "ungebrochen" in "gebrochen" übergeht, 3) ein Schwellenwert, der Meereis brechende und nicht-brechende Wellenfelder trennt, wird verwendet, um festzustellen, wann dies geschieht, 4) zwei Arten der Dämpfung von Wellen im Eis (abhängig vom Eiszustand), die den beobachteten Ein/Aus-Schalter der Wellendämpfung darstellen. Durch die oben beschriebene Charakterisierung der Wellendämpfung und des Aufbrechens von Meereis erreichen wir eine Zwei-Wege-Kopplung zwischen Wellen und Meereis, die Rückkopplungen zwischen Wellen und Meereis ermöglicht. Dieses Modell wird dann auf eine antarktische Fallstudie für den Sommer 2019/2020 angewendet.
Wir zeigen, dass unser Modell sowohl das Wellenfeld innerhalb der Randeiszone als auch deren Entwicklung sehr zuverlässig simulieren kann. Diese Ergebnisse sind ein weiterer Beweis für die Gültigkeit des beobachtungsbasierten Ansatzes und belegen darüber hinaus, dass die im Modell verwendete Kombination mit den weiteren hier herangezogenen beobachtungsbasierten Elementen sich in der praktischen Anwendung bewährt. Darüber hinaus belegen die Ergebnisse, dass Wellen einen entscheidenden Einfluss auf die Morphologie der Randeiszone haben.

Wie oben gezeigt, sind Wellen nicht nur für sich genommen wichtig, sondern auch, weil sie andere Bereiche des Erdsystems regulieren. Der Ozean stellt hier keine Ausnahme dar. Als Nächstes betrachten wir die Auswirkungen von Wellen im Ozean, konsistent mit der auf Beobachtungen basierenden Physik des BYDBR: Wellen können durch den Prozess des Abklingens der Dünung Turbulenz und Vermischung in den Tiefen des Ozeans erzeugen. Ozeanmodelle vernachlässigen dies üblicherweise, und wir stellen hier fest, dass dies wahrscheinlich eine Quelle erheblicher systematischer Fehler in solchen Modellen ist. Dies zeigen wir durch die Implementierung dieses Effekts in das Ozeanmodell NEMO und eine systematische Untersuchung des Effekts. Wir stellen fest, dass dieser wellengekoppelte Prozess eine wichtige Quelle für die Durchmischung des

gesamten oberen Ozeans ist und dass seine Einbeziehung die Vorhersagen des Ozeans auf physikalisch konsistente Weise verbessern kann.

This page intentionally left blank.

Declaration

This is to declare that the work presented in this thesis is the original work of the author towards the Doctor of Philosophy (Ph. D.) degree, and all due acknowledgement is made in the text where other materials are used. This thesis is fewer than the maximum word limit of 100, 000 words in length, exclusive of tables, figures, bibliographies, and appendices.

Joshua S. Kousal

November, 2022

This page intentionally left blank.

Preface

The work presented in this dissertation has been carried out by the author amid enrolment in a joint Doctor of Philosophy (Ph. D.) degree at the University of Melbourne and University of Hamburg. Parts of the present dissertation have been published or submitted for publication in international conferences, workshops, and peer-reviewed journals. The author thereby declares being the primary contributing author whose contribution exceeds 50% of the work towards any of the publications listed in what follows. The author also encourages uptake of this work, and as such the code and data is made freely available where possible.

Chapter 2 is based on the following conference paper, with additional context at the beginning:

- Kousal, J., Liu, Q., Staneva, J., Behrens, A., Günther, H., Bidlot, J., & Babanin, A. V.. Introducing Observation-Based Physics Into the WAM Wave Model. *Proceedings of the ASME 2022 41st International Conference on Ocean, Offshore and Arctic Engineering*. *Volume 2: Structures, Safety, and Reliability*. Hamburg, Germany. June 5–10, 2022. V002T02A005. ASME. https://doi.org/10.1115/OMAE2022-79652

Chapter 2 code:

- A supported version will be available in future public releases of the open source ecWAM within the OpenIFS managed by ECMWF. For OpenIFS inquiries contact Marcus Koehler (Marcus.Koehler@ecmwf.int).
- A supported version will also be available in future public releases of WAM managed by Helmholtz-Zentrum Hereon. For inquiries contact Dr. Arno Behrens (arno.behrens@hereon.de).
- Additionally, an unsupported version is available on my personal Github, but this is intended only to gain an insight into what the code is and what the development has involved. Available here: https://github.com/jkousal32/WAM

Chapter 3 is based on the following research paper, with additional context at the beginning:

- Kousal, J., Voermans, J. J., Liu, Q., Heil, P., & Babanin, A. V. (2022). A two-part model for wave-sea ice interaction: Attenuation and break-up. *Journal of Geophysical Research: Oceans, 127,* e2022JC018571. https://doi.org/10.1029/2022JC018571

Chapter 3 has been presented at the following international conference:

- Kousal, J. (2021, Nov): *A two-part attenuation and break-up model for wave-sea ice interaction*. Presented at the International Workshop in the Mathematics of Sea Ice and Ice Sheets, University of Queensland, Toowoombah, Australia. View here.

Chapter 3 data:

- Kousal, J. and Voermans, J. (2022) Numerical Simulations wave fields Davis Sea, WAVEWATCHIII, January 2020, Ver. 1, *Australian Antarctic Data Centre* - doi:10.26179/e195-t836. Available at https://data.aad.gov.au/metadata/records/AAS_4593_WW3_DavisSea_2020

Chapter 3 code and explanation:

- https://github.com/jkousal32/WW3/tree/ice_break_josh

Acknowledgement

First, to Prof. Alexander Babanin: to say that this would not have been possible without you is an understatement. From our first discussions regarding supervision of an honours project in 2018, to facilitation of research abroad at ECMWF, to an impossibly cool and diverse PhD project sprinkled with interesting discussions on the best books ever written, you've been there at every point. I appreciate that you have always left space for me to find my own way in the research.

To Jean. Your enthusiasm and excitement for this project has rivalled my own. I have really appreciated your guidance, the days spent at the white board talking through the inner workings of the wave and ocean models, and the latest reports on the fresh produce coming from your garden.

To Qingxiang and Joey, I very much appreciate the time you've taken to talk through the wide range of technical and conceptual issues on all things sea ice, without which the first research chapter would have been only frazil.

To Joanna, Heinz and Arno, thanks for the motivation and technical help on the heavy task of coding BYDBR into WAM, and not being discouraged by some ugly looking results and tough-to-find bugs. I would also like to thank the rest of my supervisory committee, Prof. Ian Young, Assoc. Prof. Alessandro Toffoli, and Prof. Corinna Schrum, for their guidance and insight. Sebastian, thanks for the assistance with the Zusammenfassung.

This PhD is also a product of all the great people I've had around me over the past few years. Mum and Dad, thank you for the encouragement and foundations on all aspects of life, and the many weekends and holidays spent chasing the surf.

Bridget, thanks for everything else.

This page intentionally left blank.

Contents

Nomenclature

ECMWF	European Centre for Medium-range Weather Forecasts	
NEMO	Nucleus for European Modelling of the Ocean	(ocean model)
NEMO3.4	Version 3.4 of NEMO	(ocean model)
NEMO4.01	Version 4.01 of NEMO	(ocean model)
WW3	WAVEWATCH-III	(wave model)
WAM	European WAve Model	(wave model)
IFS	ECMWF's Integrated Forecasting System	
LIM	Louvain-la-Neuve Ice Model	(sea ice model)
SI^3	Sea Ice modelling Integrated initiative	(sea ice model)
GOTM	General Ocean Turbulence Model	(turbulence model)
MIZ	Marginal Ice Zone	
GB14	Ghantous & Babanin, 2014	(journal article)
REA14	Rodgers et al., 2014	(journal article)
BYDBR	A. V. Babanin, I. R. Young, M. A. Donelan, M. L. Banner and W. E. Rogers	(working group)
ARD	Ardhuin	(WAM source term package)
ESACCI	European Space Agency Climate Change Initiative	(satellite)
ENSO	El Niño–Southern Oscillation	
ST4	Source Term package 4	(WW3 source term package)
ST6	Source Term package 6	(WW3 source term package)
SH	Southern Hemisphere	
NH	Northern Hemisphere	
SST	Sea-Surface Temperature	
MLD	Mixed Layer Depth	
ERA5	ECMWF Re-Analysis product 5	
TKE	Turbulent Kinetic Energy	
H_S	Significant wave height	
T_P	Peak period	

List of Figures

Figure 3.4. Modelled and observed H_S following the buoys. Black markers indicate quality controlled onboard buoy H_S calculations. The inner (outer) physical range is defined as the range between the inner (outer) upper and lower bounds (see table 3.2 for simulation details).

Figure 3.5. 1D modelled and observed wave spectra. Buoy observations shown by crosses. Buoy location for February 01 can be seen in figure 3.2. The inner (outer) physical range is defined as the range between the inner (outer) upper and lower bounds (see table 3.2 for simulation details). Buoy: WB0173; time: 2020-01-30T06:48.

Figure 3.6. a) Modelled number of unbroken ice grid points for the Davis Sea region. The inner (outer) physical range is defined as the range between the inner (outer) upper and lower bounds. See table 3.2 for simulation details. **b-d)** Model simulations of unbroken sea ice for the Davis Sea region. Blue dots mark modelled solid ice for the inner upper physical bound (simulation D; see table 3.2 for simulation details). Dashed and solid black contours mark lines of 15% and 85% sea ice concentration respectively. Buoy locations are shown by the coloured crosses. Corrected Reflectance satellite imagery from the MODIS satellites are shown (https://worldview.earthdata.nasa.gov). The colour of the 'F-numbers' refers to the lines of the same colour and are to be discussed in the text.

Figure 3.7. a-b) Modelled number of unbroken ice grid points for the western and central sheets. The inner (outer) physical range is defined as the range between the inner (outer) upper and lower bounds. See table 3.2 for simulation details. **c-e)** Model simulations of unbroken sea ice for the western and central sheets. Blue and magenta dots mark modelled solid ice for the upper physical bounds (simulations D and E; see table 3.2 for simulation details). Dashed and solid black contours mark lines of 15% and 85% sea ice concentration respectively. Buoy locations are shown by the coloured crosses. Corrected Reflectance satellite imagery from the MODIS satellites are shown (https://worldview.earthdata.nasa.gov). The colour of the 'F-numbers' refers to the lines of the same colour and are to be discussed in the text.

Figure 3.8. Corrected Reflectance satellite imagery from the Aqua and Terra MODIS satellites (https://worldview.earthdata.nasa.gov). Dashed and solid black contours mark lines of 15% and 85% sea ice concentration respectively. The colour of the 'F-numbers' refer to the lines of the same colour and are to be discussed in the text.

Figure 3.9. a) Modelled number of unbroken ice grid points for the polynya barrier. The inner (outer) physical range is defined as the range between the inner (outer) upper and lower bounds. See table 3.2 for simulation details. **b-c)** Model simulations of unbroken sea ice for the polynya barrier. Blue dots mark modelled solid ice for the inner upper physical bound (simulation D; see table 3.2 for simulation details). Dashed and solid black contours mark lines of 15% and 85% sea ice concentration respectively. Buoy locations are shown by the coloured crosses. Corrected Reflectance satellite imagery from the MODIS satellites are shown (https://worldview.earthdata.nasa.gov). The colour of the 'F-numbers' refers to the lines of the same colour and are to be discussed in the text.

Figure 4.1. Mean difference in mixed layer depth between the WO_MIXING and CONTROL simulations for the months DJF (left) and JJA (right) for the years 1980-2012.

Figure 4.2. Mixed layer depth climatology for the North Pacific (left; 30-60°N; 120°E-120°W) and Southern Ocean (right; 30-90°N; all longitudes) for the WO_MIXING and CONTROL simulations for the years 1980-2012. Argo data for the period 2000-2018 is also shown.

Figure 4.3. Mean difference in sea-surface temperature between the WO_MIXING and CONTROL simulations for the months DJF (left) and JJA (right) for the years 1982-2012.

Figure 4.4. Mean difference in sea-surface temperature RMSE between the WO_MIXING and CONTROL simulations for the months DJF (left) and JJA (right) for the years 1982-2012.

Figure 4.5. Sea-surface temperature RMSE climatology for the WO_MIXING and CONTROL simulations for the years 1982-2012.

Figure 4.6. Mean difference in potential temperature between the WO_MIXING and CONTROL simulations for the months DJF (left) and JJA (right) for the years 1982-2012.

Figure 4.7. Mean difference in potential temperature RMSE between the WO_MIXING and CONTROL simulations for the years 1979-2012. **LEFT:** zonal average; **RIGHT:** vertical average (upper 200m).

Figure 4.8. Potential temperature (upper 200m) RMSE climatology for the WO_MIXING and CONTROL simulations for the years 1979-2012.

List of Tables

This page intentionally left blank.

Chapter 1:

Introduction

Ocean surface waves are an unparalleled ocean phenomenon, wreaking havoc on ocean-going vessels and spreading their tendrils into affects on many aspects of weather and climate. To understand and predict these waves, the best tool available is the third-generation spectral wave model. These models predict the growth, decay, and transformation of wind-generated waves. The modern deep-water wave physics package for such spectral models is the observation-based approach developed by A. V. Babanin, I. R. Young, M. A. Donelan, M. L. Banner and W. E. Rogers (hereafter BYDBR). This modern source term representation is based on direct field measurements of the source functions (Babanin and Young 2005; Young and Babanin 2006; Donelan et al. 2006; Babanin, Tsagareli, et al. 2007; Babanin, Banner, et al. 2007; Babanin et al. 2010; Tsagareli et al. 2010; Babanin 2012), and is therefore not subject to tuning (within confidence limits of the measurements). Furthermore, these observations revealed and/or quantified physical phenomena missing or neglected in other source packages for spectral wave models such as non-linear airflow separation (hence relative reduction of wind input at strong winds), steepness-dependent wave growth (making the wind input a weakly non-linear function of the wave spectrum), negative wind input under adverse winds, two-part wave dissipation consisting of a local in wavenumber space term and a cumulative term (which is an integral of the spectrum), a wave breaking threshold below which no breaking occurs, and swell decay due to interaction with and production of oceanic turbulence (for details on these all see Babanin et al., 2019). Of the three dominant third-generation spectral wave models, WAM, SWAN and WAVEWATCH-III, this observation-based physics is available in the latter two. These physics have demonstrated high skill across not only bulk wave parameters (e.g. significant wave height and peak wave period), but across the entire spectrum (Liu et al. 2019). These physics remain unavailable in the WAM family however, meaning that one third of the research and practical oceanographic community remain subject to the incumbent method - the semi-empirical approach of Ardhuin et al. (2010).

This observation-based physics package is concerned with global physics, and has thus targeted those environments which are of primary concern for global wave climate, i.e. open ocean, neglecting for example coastal- or polar-specific processes. Waves in these regions are important, however. The polar regions are amongst the most rapidly changing in response to climate change, and are the least well understood, contributing the largest uncertainty as to how the climate will continue to evolve over the next century. The Marginal Ice Zone comprises a particularly important part of the polar regions, and is one where ocean surface waves may be a dominant physical process. The Marginal Ice Zone is the transitional zone between open sea (typically classified as <15% sea ice concentration) and that dominated by the presence of sea ice (typically classified as >85% sea ice concentration). In this region waves and sea ice form a closely coupled system: waves govern sea ice through stress, floe break-up and wave-induced currents, whilst sea ice affects waves through attenuation and reflection. Wave-induced sea ice break-up is important here as it regulates air-sea interaction and consequently also the growth and melt of sea ice. Understanding these complex interactions and adequately representing them in our models is one piece of the jigsaw puzzle we must complete in order to better understand the polar regions in general, and therefore better understand how we can expect our planet to evolve over the coming decades.

Waves are more than just an ocean surface phenomenon, however. The orbital motion of the water particles induced by the waves extends to depths of more than 100m. This wave-orbit can stretch and amplify turbulent vortices within the ocean and impart energy to them (known as the Benilov instability mechanism). This loss of energy means attenuation of the waves, and is an important aspect of the BYDBR observation-based wave physics. This deposition of wave energy into the ocean however is routinely neglected by the ocean modelling communities. Its impact is far from negligible however, leading to additional mixing to depths of more than 100m and substantial flow on effects for oceanic heat and salinity fluxes. This is real physics that the ocean models are missing, the inclusion of which is likely to aid our understanding and prediction of the ocean.

1.1 Research objectives

This thesis is centred around observation-based wave physics. First, a major task must be undertaken that has been a long time coming: the coding, testing and validation of the BYDBR observation-based physics into the WAM wave model. This amounts to a new tool for the remaining third of the research and practical oceanographic community, and is one which frees them from the limitations within the current semi-empirical approach in WAM. This observation-based approach so far has proven extremely successful and motivates its application to other areas. One such area is the important but poorly understood Marginal Ice Zone. Through the application of this approach to this region we hope to devise a better model of wave-sea ice interaction and discover new things about the region. Lastly, we aim to address a somewhat polemic issue. A significant portion of wave orbital energy is lost to turbulence in the ocean, yet this is neglected by the ocean modelling community. Here we incorporate this additional turbulence into the ocean and study its effects. This all being considered, the specific research objectives of this thesis are:

i. Coding, testing and validation of the BYDBR observation-based wave physics into WAM. This includes both the ECMWF- and Hereon-managed versions of WAM. This therefore allows uptake by the remaining one third of the oceanographic community currently unable to use the observation-based wave physics.

ii. Compare WAM with the newly implemented BYDBR observation-based source term to WAM with the current semi-empirical approach. Focus on integrated parameters such as significant wave height and mean period. How does this translate to model performance relative to *in situ* observations?

iii. Extend the observation-based approach to wave-sea ice interactions in the Marginal Ice Zone. First, consider the most relevant recent theoretical and experimental advances in the field. Second, consider how they can be tied together and implemented within a third-generational spectral wave model in a physically consistent manner, ideally in a way that allows two-way wave-sea ice coupling and thereby feedbacks.

iv. Validate the above-outlined observation-based approach to wave-sea ice interactions in a case study. Assess for performance against *in situ* measurements from wave buoys within the sea ice. Additionally assess for performance of evolution of the sea ice using satellite imagery. What can we learn about the Marginal Ice Zone? Are waves a dominant process governing its evolution?

v. Implement the energy lost from the wave-orbital motion into an ocean general circulation model. Is this of considerable impact within the ocean? Focus on oceanic mixing and temperature. Does this improve the ocean model? Use *in situ* observations of temperature throughout the ocean, and satellite observations of surface temperature.

Chapter 2 addresses research objectives i - ii.

Chapter 3 addresses research objectives iii - iv.

Chapter 4 addresses research objectives v.

This page intentionally left blank.

This page intentionally left blank.

Chapter 2:

The Introduction of Observation-Based Physics into the WAM Wave Model

Third generation spectral wave models predict the growth, decay and transformation of wind-generated waves. WAM is one of the three dominant third-generation spectral wave models. The modern package of wave physics for spectral models, available in WAVEWATCH-III and SWAN, but not currently available in WAM, is the observation-based approach developed by A. V. Babanin, I. R. Young, M. A. Donelan, M. L. Banner and W. E. Rogers (hereafter BYDBR; see Chapter 1 for summary). This chapter documents the coding, testing and validation of BYDBR physics within WAM (see Preface for code availability)[1]. To give an indication of the scale of this task, this involved more than 500,000 lines of code. This major task has enabled the remaining third of the research and practical oceanographic community to use the BYDBR observation-based wave physics and move away from the standard semi-empirical approach. We find that the performance of WAM using BYDBR physics is roughly comparable to the standard with respect to the mean-based metrics. Considerable differences between the BYDBR physics and the standard semi-empirical approach exist, most prominently in boreal winter, with widespread reductions in the NH for significant wave height and mean wave period of ~10cm and ~0.2s respectively.

1 This chapter focuses on the ECMWF version of WAM (ecWAM), but the observation-based physics has also been made available within the Helmholtz-Zentrum Hereon version of WAM and both are available for users.

2.1. Introduction

Spectral wave models are an extremely useful tool not only for safe navigation of the seas, but also in understanding global climate through coupled interactions of waves with ocean, atmosphere and cryosphere. Different to phase-resolving models (representing individual waves), spectral wave models represent the distribution of wave energy across the frequency and direction spectrum. These models are now in their third generation. The first generation consisted of empirical relationships between winds and the wave spectrum (e.g. Pierson-Mokowitz spectrum; 1). The second generation of wave models began to employ numerical methods and mathematical equations to simulate wave physics, including a simplified representation of non-linear wave interactions (the transfer of energy between wave components; 2). The exact mathematical solution to these non-linear wave interactions has been known since 1966 in the form of the 5-dimensional Boltzmann integral (3), but is too expensive to compute within an operational wave model. The third generation of wave model is characterised by a clever approximation to this integral, known as the Discrete Interaction Approximation (DIA). The DIA then allowed an accurate and efficient computation of this non-linear term, thereby delivering us to the wave forecast models we know today. The first model of this type was the European model WAM (4). This model solves the energy balance equation (Equation 2.1, in its simplest form in case of deep water, no surface currents), thereby describing the evolution of the two-dimensional wave spectrum without any assumptions regarding the shape of the spectrum, allowing it to evolve freely (true up to the cut-off frequency, beyond which a f^{-5} tail is imposed for numerical reasons, where f denotes frequency). This remains the dominant wave model used in Europe today, and is one of the two dominant global wave models (the other being WAVEWATCH-III, discussed below).

$$\frac{\partial F}{\partial t} + \vec{V}_g \cdot \nabla F = S_{\text{nl}} + S_{\text{in}} + S_{\text{ds}} \qquad (2.1)$$

The left-hand side of Equation 2.1 represents the transport equation for the wave spectrum, whilst the right-hand side consists of the three deep-water source terms: wind input, non-linear four-wave interaction, and dissipation due to whitecapping. For the finite-depth version of WAM there are additional terms for bottom dissipation and refraction.

The right-hand side of Equation 2.1 has been an active area of development over the past forty years, with revisions of the formulation of each of these terms, as well as the addition of new source terms, most of which are environment-specific with little relevance for deep water. Swell dissipation is the exception here. This process describes the attenuation of long waves due to production of turbulence and was not accounted for in the early third-generation spectral wave models. It is now included as follows (Equation 2.2):

$$\frac{\partial F}{\partial t} + \vec{V}_g \cdot \nabla F = S_{\text{nl}} + S_{\text{in}} + S_{\text{ds}} + S_{\text{swlds}} \qquad (2.2)$$

There are two dominant physics packages for representing the latter three of these deep-water source terms. The first is described by Ardhuin et al. (5; hereafter ARD). This source term representation built on that of WAM cycle 4 (6), including novel features such as dissipation of short waves induced by that of longer waves, wind sheltering, and a non-linear, steepness-dependent swell dissipation. Although effective, this source term formulation is semi-empirical and as such carries with it the limitation that new wave model setups will require calibration (not trivial).

The modern package of wave physics for spectral models for representing the aforementioned deep-water source terms is described by Babanin et al. (7). This source term representation, developed primarily by A. V. Babanin, I. R. Young, M. A. Donelan and M. L. Banner based on direct field measurements of the source functions (8-15) and first implemented in the wave-forecast model SWAN by Rogers et al. (16) - hereafter BYDBR. It was transferred to WW3 by Zieger et al. (17)[2], and as such describes observation-based wave physics, and is not subject to the limitations arising from the empirical approach. Liu et al. (18,19) document the most recent updates and public releases of the original BYDBR source term package, including those for extreme conditions such as Tropical Cyclones and Marginal Ice Zone, as well as extensive analyses of the BYDBR 40-year hindcast (20). This wave physics package has much of its roots in the AUSWEX field campaign at

2 The ARD and BYDBR source term packages are defined respectively as ST4 and ST6 in WAVEWATCH-III. ecWAM is a different model and the source term packages are implemented differently and will have different results. For this reason we refer to them using an abbreviation of the authors names rather than the WAVEWATCH-III specific names. We note that this physics is also available in SWAN public releases since 2020.

Lake George, Australia (21,22), and incorporates physical phenomena previously missing in spectral wave models, including non-linear airflow separation, steepness-dependent wave growth, negative wind input under adverse winds, two-part wave dissipation consisting of a local and a cumulative term, a wave breaking threshold below which no breaking occurs, and swell decay due to oceanic turbulence production. Note that ARD also represents some of these phenomena albeit in different forms[3]. BYDBR physics was first implemented and tested within SWAN (a third-generation wave model with a coastal focus). This was followed by extensive development of this source term package within WAVEWATCH-III (23; hereafter WW3), demonstrating high skill across not only bulk wave parameters (e.g. significant wave height and wave period), but across the entire spectrum (19). This source term package has never been made available in WAM however, meaning that WAM continues to remain subject to empirical limitations. The introduction of BYDBR into WAM addresses this, and is the focus of this work.

3 A list of physical phenomena encompassed by BYDBR is provided in the Introduction, and expanded upon in Materials and Methods. This is a list of physical phenomena that have often been neglected, which the BYDBR source term package now represents, many of which have been pioneered by BYDBR. This is not a list of features that are unique to BYDBR however, with both BYDBR and ARD advancing simultaneously. Here we outline some similarities and differences between physical phenomena represented within BYDBR and ARD.

In Materials and Methods we outline two features of the wind input BYDBR source term formulation: (i) non-linear air-flow separation, and (ii) a steepness dependent wave growth rate. ARD does not feature either of these. Materials and Methods also outlines three features of dissipation due to breaking represented in BYDBR: (i) a steepness-dependent wave-breaking threshold, below which waves will not break, (ii) cumulative dissipation, and (iii) non-linearity of dissipation for strong winds. ARD includes representations of the first two of these physical features, albeit it in a different form, but not the third. Both BYDBR and ARD represent swell dissipation, although BYDBR attributes this to energy converted to oceanic turbulence, and ARD attributes this to energy converted to atmospheric turbulence. Young et al. (26) demonstrates the two to be functionally identical. We also note that there is one physical feature represented in ARD and not in BYDBR: the reduction of energy input for short waves due to the wind shelter provided by longer waves.

2.2. Materials and methods

2.2.1. Model

The wave model used here is ecWAM (CY47R3): The version of WAM operated and developed by the European Centre for Medium-Range Weather Forecasts (hereafter ECMWF). For this study, ecWAM is run in standalone mode on a global 28 km grid with 36 frequency bins and 36 directional bins with 6 hourly winds from ECMWF analyses. This is a research configuration in which the impact of coupling ecWAM to the rest of the Integrated Forecasting System (IFS) is not activated. In operational mode, ecWAM is actively coupled to the atmosphere and the ocean circulation components of ECMWF Earth System Model (6).

Within ecWAM the two wave physics choices available are WAM cycle 4 (24; IPHYS=0) and ARD (5; IPHYS=1). Here we document the introduction of BYDBR wave physics into ecWAM (IPHYS=2). Within the ecWAM code, the module which is responsible for the implicit integration of the source terms of Equation 2.2 is called IMPLSCH. This module calls all relevant sub-modules, including for the wind input source term (SINPUT), the dissipation source term (SDISSIP), for identifying the cut-off frequency (FRCUTINDEX), for imposing a f^{-5} tail above this cut-off frequency (IMPHFTAIL), and for calculating the atmosphere-wave-ocean fluxes and stresses (AIRSEA, STRESSO). Figure 2.1 shows a diagrammatic representation of this. Here we will introduce equivalent modules for BYDBR physics by similar names but with the additional "_BYDBR" suffix (Fig. 2.1).

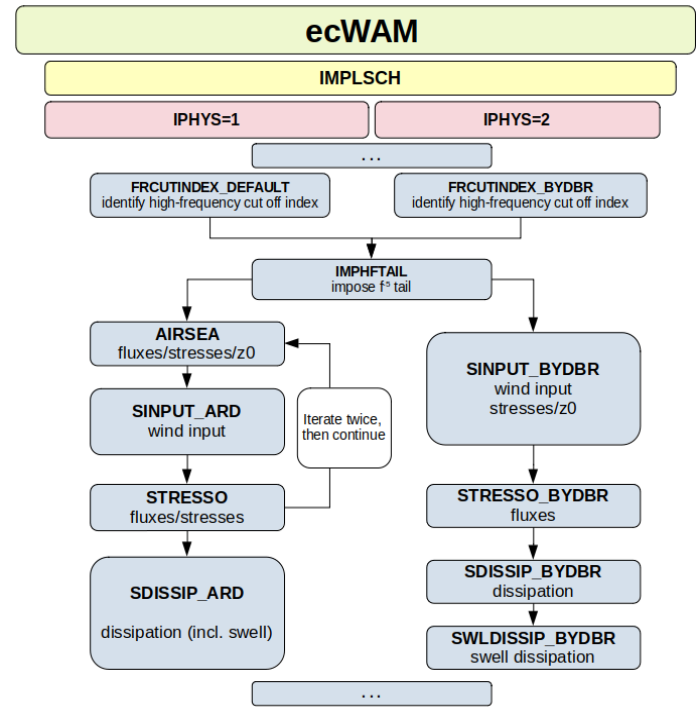

Figure 2.1. A diagram depicting the updated logic of ecWAM. On the left is the standard ARD source term representation (IPHYS=1), and on the right is the BYDBR physics implementation (IPHYS=2).

The wind input source term formulation for BYDBR includes novel physical features previously not accounted for, including full air-flow separation leading to a relative reduction of wind input for conditions of strong winds/steep waves, and a steepness dependent wave growth rate, accounting for non-linear behaviour of wind input. This is accounted for in the new ecWAM module "SINPUT_BYDBR". To account for differing biases between wind products, wave models typically use a parameter to scale the wind by. This is represented within SINPUT_BYDBR as CDFAC. The wind input source term for ARD consists of a double-iteration of AIRSEA, SINPUT_ARD and STRESSO. This is replaced by just one iteration of SINPUT_BYDBR for IPHYS=2. Integrated spectral quantities are computed by the new ecWAM module "STRESSO_BYDBR".

Dissipation is dictated by two distinct physical phenomena: dissipation due to breaking (whitecapping; S_{ds} in Equation 2.2), and dissipation due to swell attenuation (swell dissipation; S_{swlds} in Equation 2.2). The whitecapping dissipation source term for BYDBR includes the

following new features: (i) a steepness-dependent wave-breaking threshold, below which waves will not break, with breaking probability then a function of the degree of exceedance above this threshold, (ii) cumulative dissipation, whereby longer waves can induce breaking and dissipation of shorter waves, and (iii) non-linearity of dissipation for strong winds. This is represented as new ecWAM module "SDISSIP_BYDBR". The swell dissipation source term for BYDBR accounts for the conversion of wave energy into turbulent kinetic energy in the ocean, most dominant for long waves but active across the entire spectrum. This is represented as a function of wave steepness, peak wave number and sea-surface variance, and encapsulated by the new ecWAM module "SWLDISSIP_BYDBR". In the ARD source term representation, dissipation due to breaking and swell attenuation are both represented in the module SDISSIP_ARD. This is replaced by SDISSIP_BYDBR and SWLDISSIP_BYDBR for IPHYS=2.

BYDBR also uses a different cut-off frequency (the frequency which separates the freely evolving part of the spectrum from that which is prescribed a f^{-5} tail). The index of this frequency is identified by the new ecWAM module "FRCUTINDEX_BYDBR", which replaces the default module FRCUTINDEX_DEFAULT for IPHYS=2. Numerical tests show the cut-off frequency given by FRCUTINDEX_BYDBR generally to be higher than that given by FRCUTINDEX_DEFAULT (i.e. allowing the freely-evolving spectrum to extend further into the higher frequencies in BYDBR)[4]. The spectrum is prescribed with an f^{-5} tail beyond this cut-off frequency for both BYDBR and ARD by the module IMPHFTAIL.

Within each of these new ecWAM modules, the implementation of the BYDBR source terms generally follows their representation within WW3. For a comprehensive outline of the formulation of each of these source terms refer to section 2.3.11 of the WW3 documentation (23).

4 Note that the cut-off frequency used for ARD (as determined by FRCUTINDEX_DEFAULT) is specific to the ecWAM implementation of ARD. This frequency is selected such that the cumulative term in S_{ds} is not computed. This computation is expensive and was deemed to not sufficiently improve performance to justify the cost.

2.2.2. Experiments

A series of simulations are run using BYDBR physics in ecWAM (IPHYS=2). To determine which value of the coefficient within BYDBR that accounts for differing wind biases (CDFAC) is most appropriate for ECMWF analysis winds, we run a series of one year hindcasts with differing values of CDFAC (20180605 - 20190615). The first month of model data is discarded to account for model spin up, making the analysis period 20180705 -20190615. We also run an experiment using ARD physics over the same period for comparison. These experiments are summarised in table 2.1.

To determine comparative performance of each experiment, they were assessed using linear regression tests against *in situ* observations from ECMWF data set prepared for the Lead Centre for Wave Forecast Verification activities (https://confluence.ecmwf.int/display/WLW/Verification+results).

Table 2.1. Summary of RMSE results of linear regression for each BYDBR experiment. All experiments are 0.25° global, analysed from 20180705 - 20190615. Experiment refers to the experiment ID assigned by the IFS operating system. CDFAC is the coefficient within BYDBR to account for differing wind biases.

Experiment	**CDFAC**	**Physics**	**HS RMSE**	**TP RMSE**
			significant wave height	peak period
			[m]	[s]
ho58	1.08	0	0.261	2.16
ho5h	1.06	0	0.254	2.14
ho5j	1.04	0	0.250	2.12
ho5k	1.02	0	0.248	2.10
ho8n	1.00	0	0.248	2.08
hot9	0.98	0	0.260	1.97
hojj	0.92	0	0.288	1.96

Table 2.2. Comparison of RMSE: BYDBR (CDFAC=1.00) vs ARD. All experiments are 0.25° global, and are analysed from 20180705 - 20190615. Experiment refers to the experiment ID assigned by the IFS operating system. ARD and BYDBR indicate the source term packages. CDFAC is the coefficient within BYDBR to account for differing wind biases. RMSE difference given as percentage, calculated as 100% * (ho8n - ho57) / ho57.

Experiment	**CDFAC**	**Physics**	**HS RMSE**	**TP RMSE**
			significant wave height	peak period
			[m]	[s]
ho57	–	ARD	0.245	2.01
ho8n	1.00	BYDBR	0.248	2.08
RMSE difference (BYDBR vs. ARD)			+1%	+3%

2.3. Results and Discussion

2.3.1. Performance of mean-based statistics

Figure 2.2 shows the *in situ* buoy network for this period for verification (279 buoys). Figure 2.3 shows a linear regression for the 1-year BYDBR hindcast (CDFAC=1.02), against all available data for significant wave height (HS) and peak wave period (TP). BYDBR physics in ecWAM behaves sensibly across these standard wave parameters, with the line of best fit generally falling close to the line y=x (an indication of bias), and the scatter about this line remaining quite small.

The focus here is on differences between experiments however. Table 2.1 shows a summary of the results from the same analyses for each of the 1-year hindcasts. As we decrease CDFAC from its initial value (CDFAC=1.08), RMSE also decreases for both wave parameters until CDFAC=1.00, after which RMSE begins to increase again for HS. This indicates a local minimum for HS at approximately CDFAC=1.00, but not for TP, with TP RMSE continuing to fall.

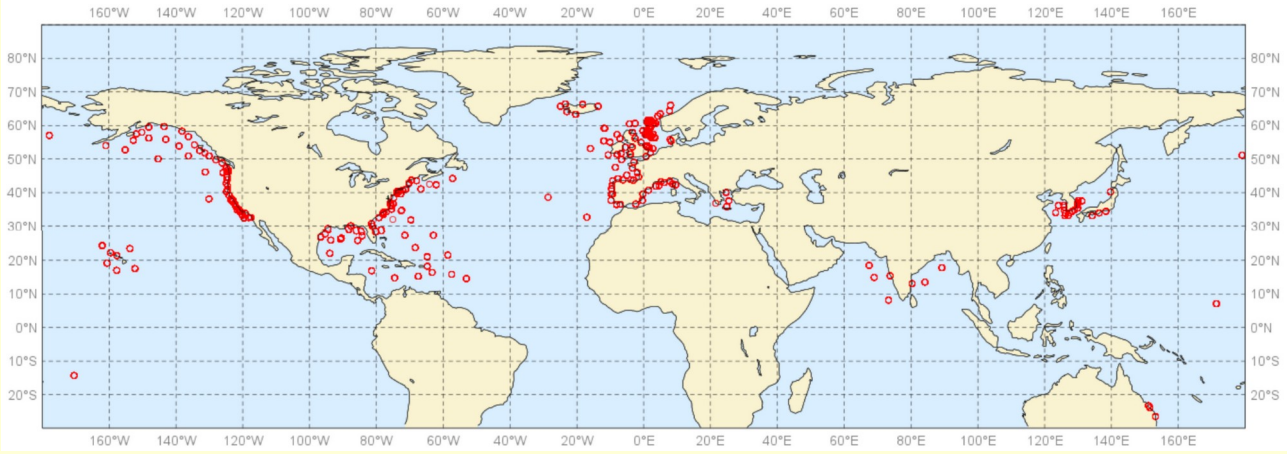

Figure 2.2. Distribution of the buoys used for verification. Figure adapted from World Meteorological Organization (WMO) Lead Centre for Wave Forecast Verification (LC-WFV) report (see https://confluence.ecmwf.int/display/WLW/WMO+Lead+Centre+for+Wave+Forecast+Verification+LC-WFV).

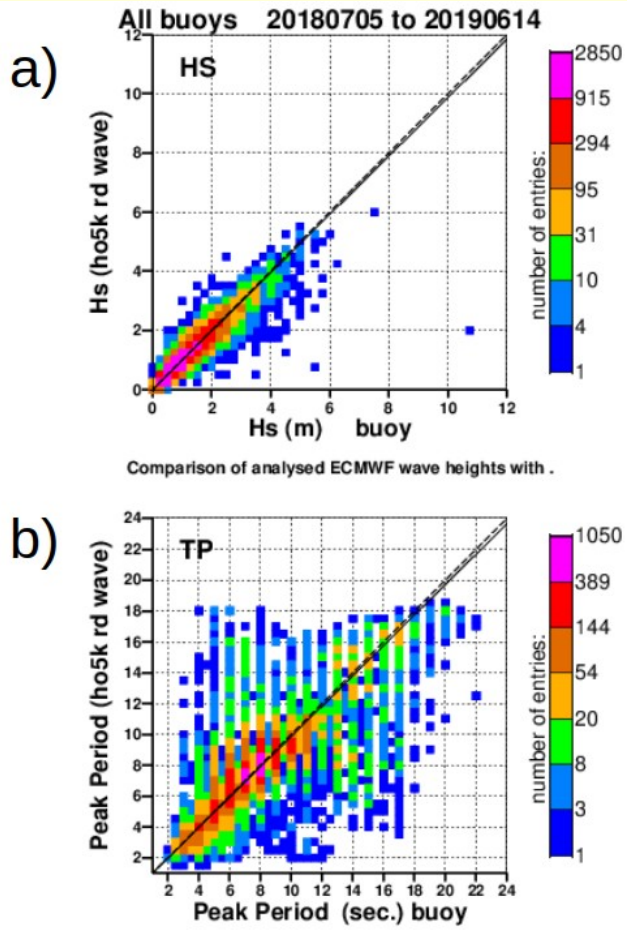

Figure 2.3. Results of linear regression analyses of BYDBR physics (CDFAC=1.02) against wave buoy data for significant wave height (a) and peak period (b). Respective number of entries are 30800 and 15649. RMSE shown in tables 2.1-2.2.

Based on these results, we settle on CDFAC=1.00 as an appropriate value. Relative to ARD, this consists of an increase in RMSE of 1% and 3% for HS and TP respectively (table 2.2). This result is consistent with that of Valiente et al. (25; a regional study using WW3 within the U. K. Met Office model). We note that Valiente et al. (25) also reports a performance increase for high energy wave states. We have not looked at this here, but intend to investigate it in the future.

2.3.2. Regional and seasonal differences

It is also of interest how BYDBR physics behaves for different regions and seasons relative to ARD in ecWAM. Figures 2.4-2.5 shows the seasonal means (JJA and DJF) of HS, Tm01 (the inverse mean wave frequency) and DIR. Beginning with boreal summer (JJA; Fig. 2.4), the global wave pattern is dominated by Southern Ocean storms. This consists of large (4-6m), long period waves (8-10s) throughout the Southern Ocean, with a maximum in the Indian Ocean quadrant. The dominant wave direction in this region is westerly (~270°), a reflection of the mid-latitude westerly winds which dominate the region. These waves propagate through much of the global ocean, and remain the dominant wave system as far north as the equator (mean wave directions S to E; 90-180°). The northern hemisphere mid latitudes are again characterised by a westerly wave direction, indicating the prevalence of strong winds in the region. The regional variances between these fields arising from the different source term representations are relatively small (maximum differences of ~5%). We see a reduction in significant wave height in the Indian Ocean quadrant of the Southern Ocean, the north-west Pacific, and the Atlantic Ocean for BYDBR, and an increase in the trade-winds regions of the east Pacific (most pronounced on the equator), the Southern Ocean surrounding New Zealand, and the north of the Indian Ocean (associated with the Indian monsoonal winds). Mean period decreases in the southern hemisphere sub-tropics (particularly in the Indian Ocean), but increases in the eastern half of the North Pacific.

For boreal winter (DJF; Fig. 2.5), we see a decrease in SH mid-latitude wave heights, and an increase in the the NH mid-latitudes, associated with the switching of the winter hemispheres (stronger winds in winter). Similarly for the mean period. This is also reflected in mean wave direction, which shows an increased prominence globally of the NH mid-latitude waves. For BYDBR relative to ARD, we see strong decreases in wave height throughout the NH mid-latitudes, with smaller increases in the SH mid-latitudes and the tropical Pacific. The changes to mean period are dominated by decreases in the tropics and sub-tropics. The differences between BYDBR and ARD are much more prominent for boreal winter. We see significant decreases in wave height in the Northern Pacific and the entire Atlantic Ocean for BYDBR. Conversely, there are increases across much of the SH (albeit of smaller magnitude), most pronounced in the equatorial Eastern Pacific. There is also clear reduction in mean period for essentially all regions north of 30°S, most pronounced in the NH mid-latitude storm belt and the Atlantic, accompanied by an anti-clockwise

rotation of mean wave direction suggesting an increased dominance of Southern Ocean wave energy.

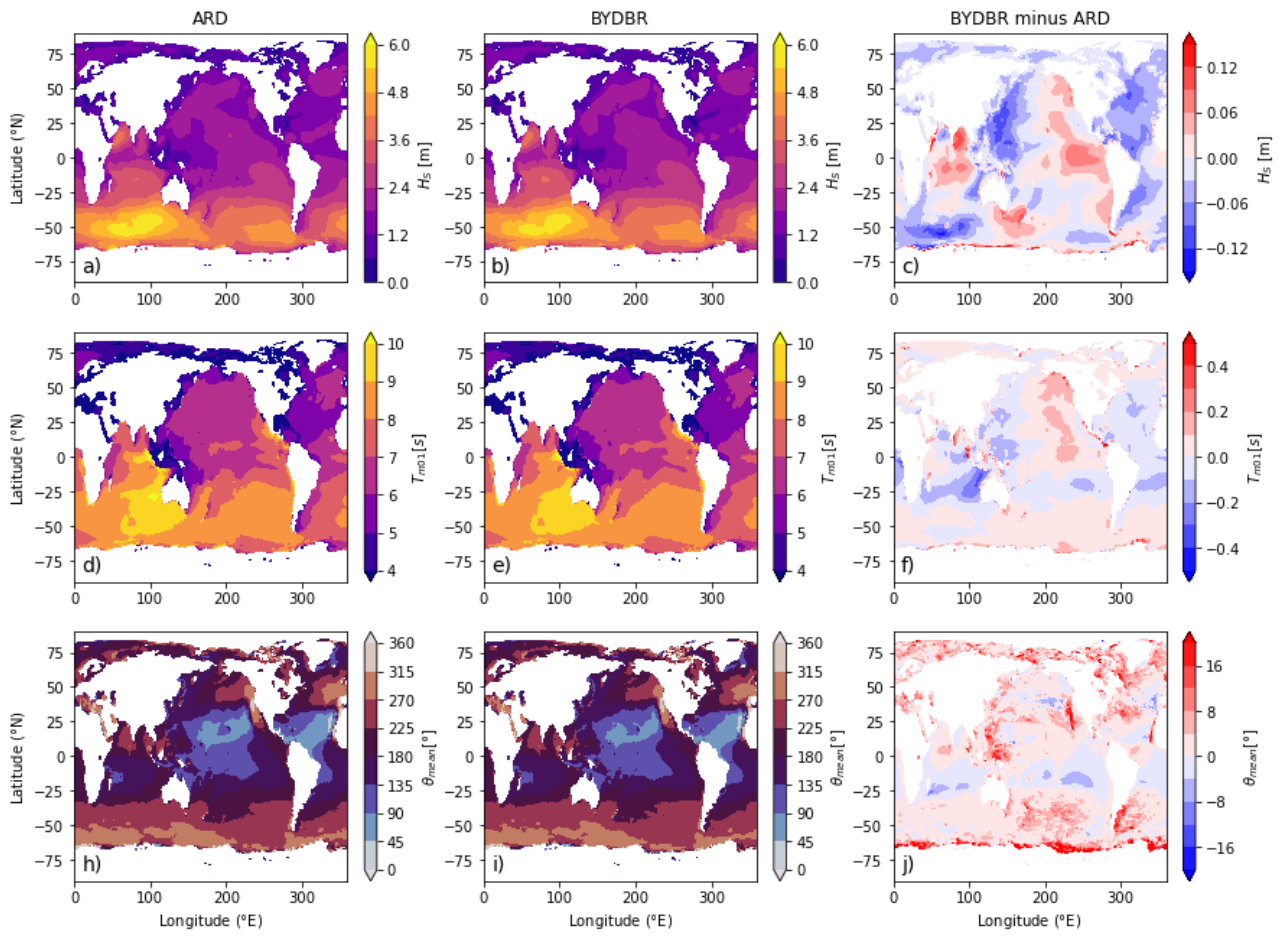

Figure 2.4. Boreal summer means (JJA) for the 1 year hindcast for significant wave height (a-b), inverse mean wave frequency (d-e) and mean wave direction (h-i), shown for ARD (a,d,h) and BYDBR source term representations (CDFAC=1.02; b,e,i). The difference is shown in the third column (BYDBR minus ARD; c,f, j).

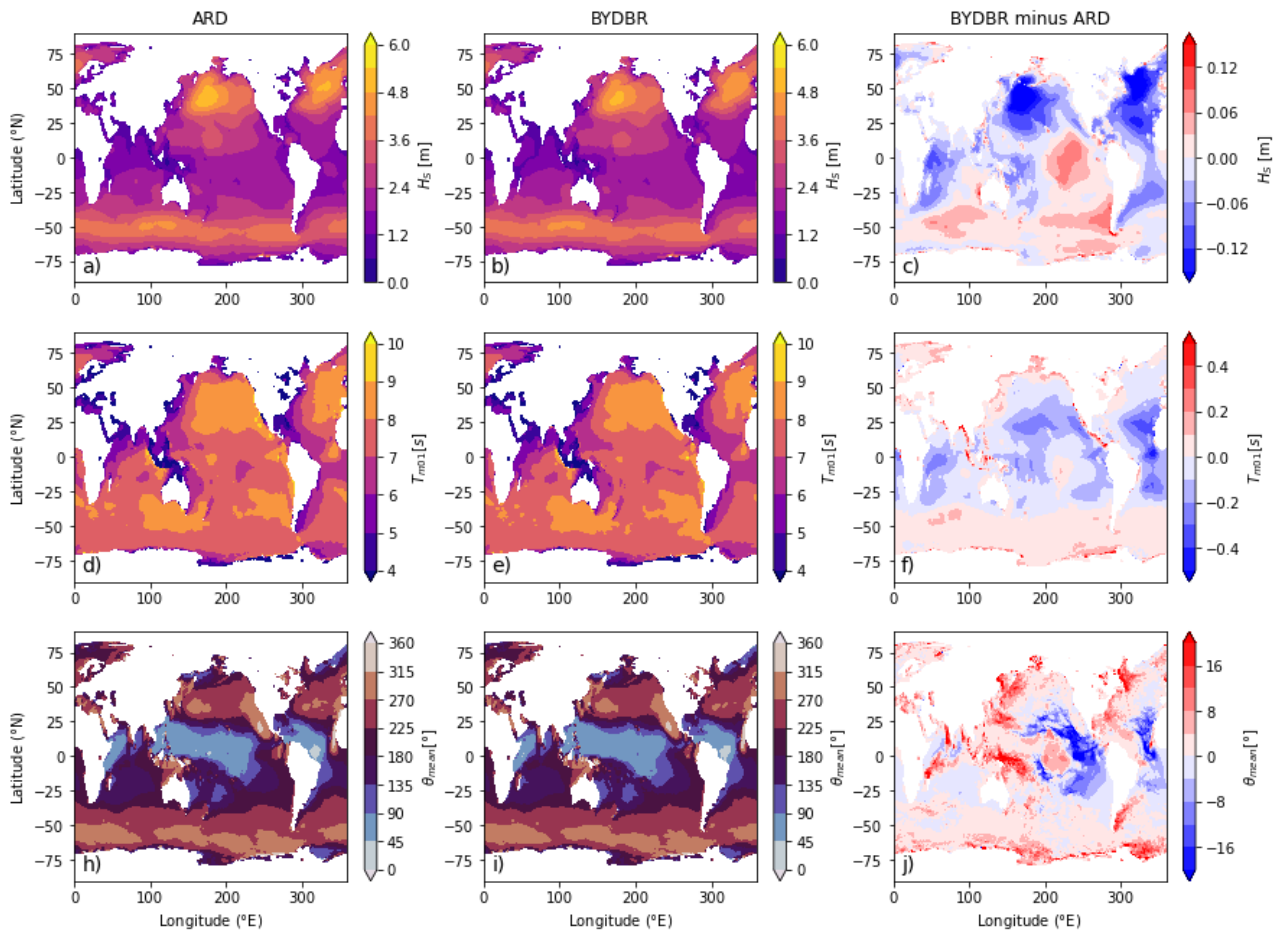

Figure 2.5. Boreal winter means (DJF) for the 1 year hindcast for significant wave height (a-b), inverse mean wave frequency (d-e) and mean wave direction (h-i), shown for ARD (a,d,h) and BYDBR source term representations (CDFAC=1.02; b,e,i). The difference is shown in the third column (BYDBR minus ARD; c,f, j).

2.4. Conclusions and future research

This work documents the coding, testing and validation of the observation-based wave physics of A. V. Babanin, I. R. Young, M. A. Donelan, M. L. Banner and W. E. Rogers (BYDBR) within the WAM wave model. With over 500,000 lines of code, this was no menial task, and has laid a key stepping stone for future research with observation-based wave physics. See Preface for code availability.

There are significant differences in wave climatology between BYDBR and the standard representation, Ardhuin et al. (5; ARD). In BYDBR we see widespread reductions in the NH for wave height and mean period of ~10cm and ~0.2s respectively (corresponding to differences of approximately 5%), most prominent in boreal winter. This is associated with an anti-clockwise rotation of mean wave direction, meaning increased dominance of waves from the Southern Ocean. In other regions, particularly the eastern Pacific and the Southern Ocean, we see increases of almost the same magnitude. Despite these differences in wave climatology, we find that performance of BYDBR physics is comparable to the highly tuned operational standard of ARD.

This implementation has opened the gate to an expansive area of research. The most pressing of these are outlined here:

1. What are the underlying cause of the differences between the two wave packages?
2. We focused on mean wave climatology. How do the two wave packages differ in the extremes? e.g. 90th and 99th percentile wave heights. This is particularly pertinent with the move towards higher resolutions, where we will actually be able to capture extremes better. This is now being explored by collaborators on the regional scale within the context of the Black Sea, work made possible by this thesis. In the future we plan to explore this on the global scale also.
3. We used a network of *in situ* buoys to assess accuracy of WAM using these two packages. Whilst there are many buoys in this network, much of the worlds ocean remains without wave buoys and are therefore under-represented in this analysis (in fact, the buoys are almost exclusively in coastal regions). Using satellite observations we could actually properly sample the global ocean, and therefore better understand the biases in WAM wave climatology for each of the two packages.

4. This work was done using the one-way coupled setup of the ecWAM wave model (i.e. the waves are controlled by the wind, but the wind is unaware of the waves). This is the standard approach for wave modelling. Uniquely, ecWAM exists fully coupled to the atmosphere as part of ECMWF's forecasting system (IFS). The next step is to utilise this coupled version of ecWAM to achieve two-way wave-atmosphere coupling for the BYDBR observation-based physics. This work, although not included in this thesis, is well underway. As a first step, we are adapting the existing approach used to two-way couple the ARD wave physics to the atmosphere through the Charnock parameter, which utilises the concept of the drag and is implemented through an oceanic roughness length. Later we will explore coupling through stresses, which is much closer to the physics and brings the advantage of being additive (unlike roughness length). The BYDBR observation-based physics has never been coupled two-way to the atmosphere. Its implementation here in ecWAM has now opened the door to this possibility. What the result will be is perhaps the most interesting question of them all.

2.5. References

1. Pierson, W.J., and Moskowitz, L.1964. "A proposed spectral form for fully developed wind seas based on the similarity theory of S.A. Kitaigorodskii." Journal of Geophysical Research 69 (24): 5181-5190.
2. Tucker, M.J., and Pitt, E.G. 2001. "Second-generation wave model developments at the UK Met Office." Coastal Engineering 43 (1-2): 37-48.
3. Zakharov, V.E., and Filonenko, N.N. 1966. "On the energy exchange between gravity waves on the surface of a finite-depth fluid." Journal of Applied Mechanics and Technical Physics 7(2): 83-89.
4. WAMDI Group, A. 1988. “The WAM Model – a Third Generation Ocean Wave Prediction Model.” Journal of Physical Oceanography 18 (12): 1775–1809.
5. Ardhuin, F., W. E. Rogers, A. V. Babanin, J. Filipot, R. Magne, A. Roland, A. van der Westhuysen, et al. 2010. “Semiempirical Dissipation Source Functions for Ocean Waves. Part I: Definition, Calibration, and Validation.” Journal of Physical Oceanography 40: 1917–41.
6. European Centre for Medium-Range Weather Forecasts. 2021. “‘Part VII: ECMWF WAVE MODEL’ in IFS DOCUMENTATION CY47R3.” Shinfield Park, Reading, RG2 9AX, England.
7. Babanin, A.V., I. Young, M. Donelan, W.E. Rogers, S. Zieger, and Q. Liu. 2019. Source Terms: . In WAVEWATCH III® Development Group (WW3DG), The, 2019: User manual and system documentation of WAVEWATCH III® version 6.07. Tech. Note 333, NOAA/NWS/NCEP/MMAB, College Park, MD, USA, 55-64
8. Babanin, Alexander V., and Ian R. Young. 2005. “Two-Phase Behaviour of the Spectral Dissipation of Wind Waves.” In Proceedings Ocean Waves Measurement and Analysis, Fifth International Symposium WAVES2005, 3-7 July, 2005, Madrid, Spain, Sponsors: CEDEX (Spain) and CORPI of ASCI (USA), paper no.51, 11p
9. Young, Ian R., and Alexander V. Babanin. 2006. “Spectral Distribution of Energy Dissipation of Wind-Generated Waves Due to Dominant Wave Breaking.” Journal of Physical Oceanography 36 (3): 376–94.

10. Donelan, M. A., Alexander V. Babanin, Ian R. Young, and M. L. Banner. 2006. “Wave Follower Measurements of the Wind Input Spectral Function. Part 2. parameterisation of the Wind Input.” Journal of Physical Oceanography 36 (8): 1672–88.
11. Babanin, Alexander V., K. N. Tsagareli, Ian R. Young, and D. J. Walker. 2007. “Implementation of New Experimental Input/Dissipation Terms for Modeling Spectral Evolution of Wind Waves.” In Proceedings of the 10th International Workshop on Wave Hindcasting and Forecasting and Coastal Hazards, Oahu, Hawaii, November, 11-16, 2007, Sponsors: U.S. Army Engineer Research and Development Center’s Coastal and Hydraulics Laboratory, Environment Canada, WMO/IOC Joint Technical Commission for Oceanography and Marine Meteorology (JCOMM), 12p
12. Babanin, Alexander V., M. L. Banner, Ian R. Young, and M. A. Donelan. 2007. “Wave Follower Measurements of the Wind Input Spectral Function. Part 3. parameterisation of the Wind Input Enhancement Due to Wave Breaking.” Journal of Physical Oceanography 37 (11): 2764–75. https://doi.org/10.1175/JPO3147.1.
13. Babanin, A. V., Tsagareli, K. N., Young, I. R. & Walker, D. J. 2010. “Numerical Investigation of Spectral Evolution of Wind Waves. Part 2. Dissipation Function and Evolution Tests.” Journal of Physical Oceanography 40 (4): 667–83.
14. Tsagareli, K. N., A. V. Babanin, D. J. Walker, and I. R. Young. 2010. “Numerical Investigation of Spectral Evolution of Wind Waves. Part I: Wind-Input Source Function.” Journal of Physical Oceanography 40 (4): 656–66. https://doi.org/10.1175/2009JPO4345.1.
15. Babanin, Alexander V. 2012. “Swell Attenuation Due to Wave-Induced Turbulence.” In Proceedings of the ASME 2012 31st International Conference on Ocean, Offshore and Arctic Engineering OMAE2012, July 1-6, 2012, Rio de Janeiro, Brazil, ISBN 978-0-7918-4489-2, 5p. https://doi.org/10.1115/OMAE2012-83706.
16. Rogers, W. Erick, Alexander V. Babanin, and David W. Wang. 2012. “Observation-Consistent Input and Whitecapping Dissipation in a Model for Wind-Generated Surface Waves: Description and Simple Calculations.” Journal of Atmospheric and Oceanic Technology 29 (9): 1329–46. https://doi.org/10.1175/JTECH-D-11-00092.1.
17. Zieger, Stefan, Alexander V. Babanin, W. Erick Rogers, and Ian R. Young. 2015. “Observation-Based Source Terms in the Third-Generation Wave Model WAVEWATCH.” Ocean Modelling 96 (December): 2–25. https://doi.org/10.1016/j.ocemod.2015.07.014.

18. Liu, Qingxiang, Alexander V. Babanin, Yalin Fan, Stefan Zieger, Changlong Guan, and Il-Ju Moon. 2017. “Numerical Simulations of Ocean Surface Waves under Hurricane Conditions: Assessment of Existing Model Performance.” Ocean Modelling 118: 73–93.
19. Liu, Qingxiang, W. Erick Rogers, Alexander V. Babanin, Ian R. Young, Leonel Romero, Stefan Zieger, Fangli Qiao, and Changlong Guan. 2019. “Observation-Based Source Terms in the Third-Generation Wave Model WAVEWATCH III: Updates and Verification.” Journal of Physical Oceanography 49 (2): 489–517. https://doi.org/10.1175/JPO-D-18-0137.1.
20. Liu, Qingxiang, Alexander V. Babanin, W. Erick Rogers, Stefan Zieger, Ian R. Young, Jean-Raymond Bidlot, Tom Durrant, et al. 2021. “Global Wave Hindcasts Using the Observation-Based Source Terms: Description and Validation.” Journal of Advances in Modeling Earth Systems 13 (8): 1–38. https://doi.org/10.1029/2021ms002493.
21. Donelan, M. A., Alexander V. Babanin, Ian R. Young, M. L. Banner, and C. McCormick. 2005. “Wave Follower Field Measurements of the Wind Input Spectral Function. Part I. Measurements and Calibrations.” Journal of Atmospheric and Oceanic Technology 22 (7): 799–813.
22. Young, Ian R., M. L. Banner, M. A. Donelan, Alexander V. Babanin, W. Kendall Melville, Fabrice Veron, and C. McCormick. 2005. “An Integrated System for the Study of Wind Wave Source Terms in Finite Depth Water.” Journal of Atmospheric and Oceanic Technology 22 (7): 814–28.
23. The WAVEWATCH III Development Group (WW3DG). 2019. “User Manual and System Documentation of WAVEWATCH III Version 6.07.” NOAA / NWS / NCEP / MMAB Technical Note, no. 333.
24. Bidlot, Jean-Raymond, Peter A. E. M. Janssen, and S. Abdalla. 2007. A Revised Formulation of Ocean Wave Dissipation and Its Model Impact. ECMWF Tech. Memo. 509. ECMWF, Reading, United Kingdom. http://www.ecmwf.int/publications/.
25. Valiente, Nieves G., Andrew Saulter, John M. Edwards, Huw W. Lewis, Juan M.Castillo Sanchez, Diego Bruciaferri, Christopher Bunney, and John Siddorn. 2021. “The Impact of Wave Model Source Terms and Coupling Strategies to Rapidly Developing Waves across the North-west European Shelf during Extreme Events.” Journal of Marine Science and Engineering 9 (4). https://doi.org/10.3390/jmse9040403.

26. Young, I. R., Alexander V. Babanin, and S. Zieger. 2013. “The Decay Rate of Ocean Swell Observed by Altimeter.” Journal of Physical Oceanography 43 (11): 2322–33. https://doi.org/10.1175/JPO-D-13-083.1.

This page intentionally left blank.

This page intentionally left blank.

Chapter 3:

Coupled Interactions Between Waves and Sea Ice in the Marginal Ice Zone

The observation-based approach to wave physics has proven so far extremely successful, and motivates its application to other areas. One such area is the important but poorly understood Marginal Ice Zone. Here, waves and sea ice form a closely coupled system: waves govern sea ice through stress, floe break-up and wave-induced currents, whilst sea ice affects waves through attenuation and reflection. Wave-induced sea ice break-up is particularly important as it can regulate air-sea interaction and consequently also regulate the growth and melt of sea ice. This coupled nature is complex and generally, especially at the large scale, neglected in modelling of the polar climate system. Here we explore a novel way of coupling through wave-induced ice break-up, and conduct a case study for the Antarctic summer of 2019/2020. Our modelling approach builds upon previous investigations of wave-sea ice interaction and can be summarised as follows: 1) sea ice takes a binary form, either 'broken' or 'unbroken', 2) waves may break sea ice, transitioning it from unbroken to broken, 3) a threshold separating breaking and non-breaking wave fields is used to identify when this occurs, 4) two modes of attenuation for waves in ice (dependent upon the ice state), representing the observed on/off switch in wave attenuation. By characterising wave attenuation and sea ice break-up as described above, we achieve a two-way wave-sea ice coupling, thereby allowing wave-sea ice feedbacks. We demonstrate that our model can simulate both the wave field in and the evolution of the Marginal Ice Zone. These results demonstrate the validity of the theoretical and empirical works included here, as well as their suitability to operate in combination. Furthermore, these results substantiate that waves have a critical influence on the morphology of the Marginal Ice Zone.

3.1. Introduction

Waves influence the shape and size of ice floes through ice break-up (Langhorne et al., 1998) and govern the state of initial sea-ice congelation (frazil versus nilas) and influence its evolution (i.e., pancake ice; Shen & Ackley, 1991). Waves also impart momentum to the ice as they are attenuated (Longuet-Higgins, 1977; Longuet-Higgins & Stewart, 1962), pushing the ice in the direction of wave propagation and affect ice drift (Feltham, 2005; McPhee, 1980; Williams et al., 2017). Stopa et al. (2018) show wave action to be the dominant control of sea-ice translation drift along the outer edge of the Southern Ocean sea-ice area, the Antarctic Marginal Ice Zone (MIZ). There are also numerous indirect effects of waves on ice, such as modified air-sea heat fluxes and enhanced lateral melt associated with break-up of sea ice (Steele, 1992).

Sea ice also governs the wave evolution. Sea ice-induced wave attenuation may be broadly classed into two categories: scattering and dissipation. The former is described by a partial reflection of waves at the boundaries of ice floes, broadening the distribution of wave direction. Scattering by multiple ice edges directly contributes to the exponential decay of the forward-going wave energy. The latter category, dissipation, describes processes which result in loss of energy from the waves. This includes, but is not limited to, internal friction due to ice viscosity, ice fracture (e.g., Squire, 2020), overwash (Toffoli et al., 2015) and under-ice turbulence (e.g., Voermans et al., 2019). The relevance and even more the dominance of each of these processes and categories are essentially unknown. The case studies of Kohout & Meylan (2008) and Montiel et al. (2016, 2018) suggest dissipation to be the more important attenuation mechanism. Within the dissipation framework, Rogers et al. (2021) identified at least three theoretical models consistent with the attenuation observed across a range of conditions. Other studies suggest that dissipation only dominates for long waves, with scattering the dominant attenuative process for short waves (Wadhams et al., 1986; Sutherland & Gascard, 2016).

It is clear that more research is needed on which processes dominate under any given circumstances. In the meantime, we need a workable solution. Many previous solutions have attempted to include all possible physical processes (despite questions regarding their relevance; each often introducing new unknown parameters), with the consequence that our wave-sea ice

interaction models have become burdened with increasing complexity and more unknowns. These unknowns are often used as tuning parameters, meaning such empirical models will need to be re-run each time the wave or ice conditions change, thereby limiting their broader relevance.

Many previous solutions also neglect two-way coupling between waves and sea ice. As soon as we have both waves and sea ice evolving together, it is insufficient to only consider the effect of waves on ice, or of ice on waves. The case studies of Collins et al. (2015) and Ardhuin et al. (2020) both show a rapid evolution of waves and sea ice over the period of a few hours, with the sea ice breaking in response to the waves, and the waves within the sea ice rapidly growing in response to this changed ice state. Both report two distinct phases in attenuation of waves by sea ice: strong attenuation under unbroken ice conditions, and unimpeded propagation under broken ice conditions. Wave attenuation reduces by at least an order of magnitude once the ice is broken (Voermans et al., 2021), hence the waves can propagate further and break more sea ice.

Interactions between waves and sea ice carry implications for many other aspects of the polar climate. For example, when the sea ice breaks there is a direct connection between ocean and atmosphere, meaning heat fluxes can transfer between the two. In the ice melt season (typically warm air), sea ice break-up leads to a warming of the ocean surface and a consequent acceleration of ice melt, including lateral melting (Bateson et al., 2020; Boutin et al., 2020). This melting is further accelerated by the decrease in albedo (and resultant increase in solar radiation absorbed) due to the exposure of dark ocean below the ice (Curry et al., 1995). As a result, there is more open water, waves can have longer fetches and grow higher, and further break the weakened ice in MIZ (Thomson & Rogers, 2014). Li et al. (2021) shows that this wave-induced sea ice break-up can accelerate melting in this season. In the ice growth season (typically cool air), sea ice break-up leads to a rapid cooling of the ocean surface, enabling the surface to refreeze after the ice floes spread to larger areas, thereby suppressing wave generation and attenuating existing waves. Li et al. (2021) shows that this wave-induced sea ice break-up can lead to increases in sea ice concentration and thickness in this season.

Insufficient knowledge regarding the underlying physics (as well as the additional complications brought by high-complexity solutions) act as motivation for a relatively simple solution to this issue, but one that still addresses the coupled nature of waves and sea ice. Here we introduce and test such a solution: a new simple

coupled model which treats sea ice mechanical integrity as binary - either 'unbroken' or 'broken'. This binary approach is motivated by the aforementioned two-phase attenuation reported by Collins et al. (2015) and Ardhuin et al. (2020). We represent this two-phase attenuation by introducing a partition into the simple two-layer dissipative attenuation model of Sutherland et al. (2019). The binary switch in our model is given by the critical threshold of the ice-breakup parameter of Voermans et al. (2020). Although simple, we show in this study that our model can capture the coupled nature of the wave-sea ice system through characterisation of the critical feedback between ice-induced wave damping and the wave-induced sea ice break-up.

3.2. Methods

A nested version of the third-generation spectral wave model, WAVEWATCH-III, is used (hereafter WW3; WW3DG, 2019). Wave information is passed from the global coarse-resolution grid (0.5°) to the Davis Sea (East Antarctica) regional high-resolution grid (0.1°; Fig. 3.1). The global grid domain is unbounded in longitude (with circular boundary conditions) and bounded by 80°S-80°N, whilst the Davis Sea grid domain is bounded by 60°E-80°E and 70°S-60°S. The default coastlines database in WW3 is the Global Self-consistent, Hierarchical, High-resolution Geography Database (GSHHG; Wessel & Smith, 1996). GSHHG is used for the global grid, whilst the Scientific Committee on Antarctic Research Antarctic Digital Database (SCAR ADD; Scientific Committee on Antarctic Research, 2000) coastlines are used for the Davis Sea grid. This latter database is used for its higher accuracy in Antarctic regions. The global model is forced with 0.5° sea ice concentration and 10m-wind fields from ECMWF's ERA5 reanalysis. The Davis Sea model is forced with 0.1° wind fields from ECMWF's archived forecasts, and high-resolution (3.125km) AMSR2 satellite data for ice concentration (Beitsch et al., 2013 updated; available at ftp://ftp-projects.cen.uni-hamburg.de/seaice/AMSR2). For both grids, frequency resolution increases by factor 1.1, with the first frequency at 0.045Hz, and 30 frequency bins. There are 36 directional bins (each 10°). Time step information is summarised in table 3.1.

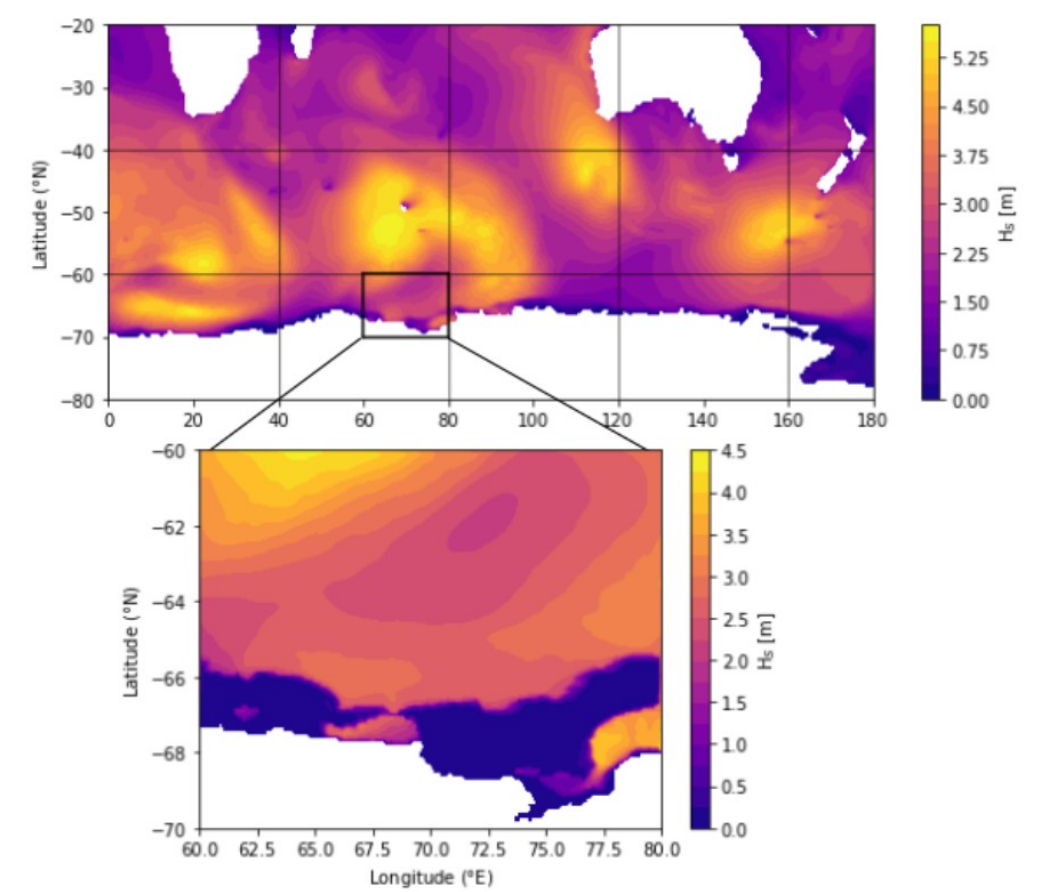

Figure 3.1. A nested set-up of WAVEWATCH-III. Wave information is passed from a global coarse-resolution grid (0.5°) to a Davis Sea regional high-resolution grid (0.1°). Snapshot of significant wave height (H_S) at 00:00, 9th Jan (2020).

For representation of sources and sinks of wave energy, we use the BYDBR observation-based source term package (ST6 in WW3; Liu et al. 2019), which represents the physical processes of wind-wave interaction, whitecapping (dissipation due to breaking) and wave-turbulence interaction (swell dissipation), and has its roots in field and laboratory observations and experiments. `CDFAC`, the ST6 parameter to account for wind field biases, is set to `CDFAC=1.08` as in Liu et al. (2021). The global grid is run from November 22, 2019 – February 14, 2020, and the Davis Sea grid is run from December 13, 2019 – February 14, 2020. Both grids are initialised with the JONSWAP spectrum (Hasselmann et al., 1973). The first month of data is discarded for the global grid, as are the first two weeks for the Davis Sea grid to ensure adequate model spin up time.

Table 3.1. Time step information for the Davis Sea and Global WW3 grids. DTMAX is the maximum global time step, DTXY is the maximum Courant–Friedrichs–Lewy (CFL) time step for x-y, DTKTH is the maximum CFL time step for spectral advection, and DTMIN is the minimum source term time step.

GRID	DTMAX	DTXY	DTKTH	DTMIN
DAVIS SEA	450s	225s	225s	10s
GLOBAL	1800s	900s	900s	10s

To describe wave attenuation through the sea ice, we use the relatively simple two-layer attenuation model of Sutherland et al. (2019;hereafter SEA19). This is a dissipative model in which wave energy is lost to internal friction within the sea ice. The attenuation through the sea ice for SEA19 is described by

$$\alpha_{SEA19} = \frac{1}{2} \Delta_0 \epsilon h_i k^2 \qquad (3.1)$$

where Δ_0 determines the boundary condition at height $-(1-\epsilon)h_i$, h_i is sea ice thickness, k is wave number, $\Delta_0 = 1$ (no-slip condition), and $0 \le \epsilon \le 1$ (relative thickness of the high-viscosity layer). Note, attenuation here follows a power dependence on frequency of n=4 ($k \sim f^2$), in fitting with the range reported by Rogers et al. (2021) of n=2 to 4.

To account for the binary nature of wave-sea ice interaction, we distinguish two regimes in the SEA19 model:

$$k_i^{IBT} = \begin{cases} k_{i\ \text{unbroken ice}}^{IBT}: & \alpha_{SEA19} \\ k_{i\ \text{broken ice}}^{IBT}: & \beta \alpha_{SEA19} \end{cases} \qquad (3.2)$$

where k_i^{IBT} is the imaginary part of the wave number representing wave growth/decay, β represents the attenuation reduction for broken sea ice (relative to unbroken sea ice cover), with $0<\beta<1$. The model is initialised with all sea ice as unbroken, meaning we are in the $k_{i\ \text{unbroken ice}}^{IBT}$ attenuation regime. To determine when the sea ice breaks, we use the non-dimensional sea ice-breakup parameter of Voermans et al. (2020; hereafter VEA20)

$$I_{\mathrm{br}} = \frac{a h_i Y}{\sigma \lambda^2} \qquad (3.3)$$

where a is wave amplitude, h_i is sea ice thickness, Y is Young's modulus, σ is flexural strength and λ is wave length. The sea ice at any point is classed as 'broken' when I_{br} exceeds its critical threshold,

$$I_{\mathrm{br\_crit}} = 0.014 \qquad (3.4)$$

thereby resulting in a transition to the 'broken ice' attenuation regime, $k_i^{IBT}{}_{\text{broken ice}}$. Assuming that the ice does not refreeze (a valid assumption for this time of year), this point then remains in the 'broken ice' attenuation regime for the remainder of the simulation.

Built upon these, we have run five simulations with our new model. A conservative range for Y and σ was chosen to describe the full range of sea ice material properties, with $\sigma \in [0.1, 0.7]$ MPa and $Y \in [0.2, 9]$ GPa (Timco & Weeks, 2010; Karulina et al., 2019). The range for the attenuation reduction coefficient for broken ice is $\beta \in [0.01, 0.1]$ (Voermans et al., 2021). Here we choose β=0.05 as being the median value. The simulations, detailed in table 3.2, are based on the combinations that result in the largest range of physical behaviour. The range of model behaviour between the 'outer lower bound' (A) and 'outer upper bound' (E) is referred to as the model's outer physical range, whilst the range between the 'inner lower bound' (B) and 'inner upper bound' (D) simulations we refer to as the model's inner physical range. The ice thickness for the inner physical range is based on a field measurement performed at the time of instrument deployment (Voermans et al., 2020). The outer physical range includes a modification to this to account for the possibility of thicker/thinner sea ice throughout other regions of the domain. The upper (lower) bounds refer to behaviour of significant wave height (H_S), and correspond with lower (higher) wave attenuation. Simulation C is our baseline simulation, with the sea ice parameters used being approximately in the middle of their physical ranges.

Table 3.2. Model simulations for the study of wave-sea ice coupled interactions. All simulations begin December 27, 2019 and finish February 14, 2020. Attenuation increases in strength from simulation A through E.

Label	Young's modulus	Flexural strength	Ice thickness	Attenuation reduction coefficient for broken ice
	Y	σ	h_i	β
	[GPa]	[MPa]	[m]	[ ]
A	9	0.1	0.55	0.01
B	9	0.1	1.1	0.01
C	6.0	0.55	1.1	0.05
D	0.2	0.7	1.1	0.1
E	0.2	0.7	2.2	0.1

To calibrate and verify WW3, we use the data described in VEA20: two ice motion loggers (Rabault et al., 2020; hereafter denoted IB) and two wave buoys (Spotter buoys from Sofar Ocean Technologies; hereafter denoted WB). Both IB and WB transmit integrated wave parameters (e.g., H_S and f_p) and wave energy density. The accuracy of the observed significant wave height is of the order of a centimetre, but varies with wave frequency (the reader is referred to Rabault et al., 2020 and Voermans et al., 2020 for more details). The instruments were deployed on landfast ice in the Davis Sea in December, 2019, along a transect perpendicular to the landfast ice edge. The first instrument was deployed about 100-200 m from the edge, and subsequent instruments were deployed a few kilometres apart. Instruments started to drift after a breakout event on the 2nd of January. The instrument tracks are shown in Figure 2.2, with the text denoting the times of their last transmissions. Note that IB1810 continued to transmit beyond 14th February 2020, the end of our study period.

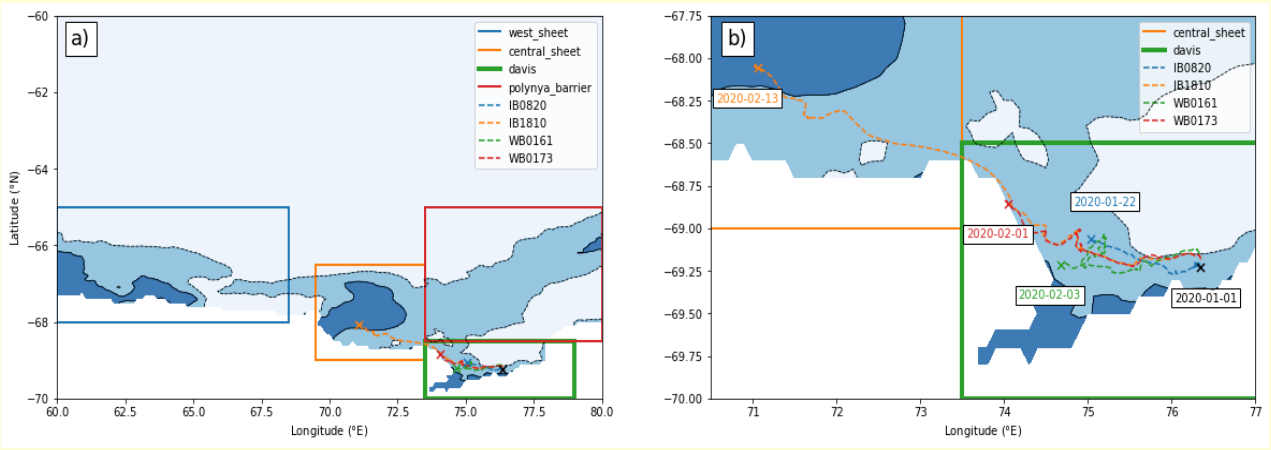

Figure 2.2. Domains and buoy tracks of the model domain **(a)**, and a close-up of the buoy tracks **(b)**. Crosses and text indicate position and date of last transmission. Dashed and solid black lines mark 15% and 85% sea ice concentration contours respectively from the AMSR2 satellite SIC product (average between January 01 and February 14).

3.3. Results

Wave and wind climate in the Davis Sea is dominated by passing low-pressure systems in the nearby Southern Ocean, with a storm passing by approximately once every week. The first significant storm in this study is on January 8. Using the two day period over which all buoys show significant wave activity (8-10 January), we calibrate the model to observations of H_S within the MIZ. This is achieved through the adjustment of ϵ (relative thickness of the highly-viscous ice layer; see Equation 1). $\epsilon = 1.2\text{e-}2$ is determined as the optimal value. Using this value, our model is then able to simulate wave behaviour throughout the MIZ over the complete simulation period (27 December 2019 to 14 February 2020).

We note here that the variable ϵ does not exist within the code for the WW3 module for the Sutherland et al. (2019) model. Instead, we rely upon the variable `HICE` to calibrate the model (Equation 3.5).

$$\texttt{HICE} = 2h_i\,\epsilon \qquad (3.5)$$

Multiple simulations are run, varying ϵ (and subsequently `HICE`). We assess the results from these simulations using regression tests. This is summarised in table 3.3, in which we see $\epsilon = 3.0\text{e-}2$ as the optimal value. Figure 3.3 demonstrates the sensitivity of the model to this parameter.

Table 3.3. Regression scores ($H_{S\,\text{model}}$ vs. $H_{S\,\text{observed}}$) for various `HICE` runs over the calibration period (Jan 8-10, 2020). `r` is the correlation coefficient and `rmse` is the root mean square error. Number of observations for each buoy: `IB0820=14; IB1810=7; WB0161=8; WB0173=8.`

HICE	ϵ	IB0820		IB1810		WB0161		WB0173		total			
										non-weighted		weighted	
e-2	e-2	r	rmse [m]	r	rmse [m]	r	rmse [m]	r	rmse [m]	r	rmse [m]	r	rmse [m]
2.5	1.1	−0.02	0.11	0.18	0.17	0.71	0.17	0.10	0.40	0.24	0.21	0.20	0.20
4.5	2.1	−0.09	0.04	0.28	0.07	0.76	0.05	0.09	0.44	0.26	0.15	0.20	0.13
5.5	2.5	−0.11	0.03	0.31	0.06	0.77	0.03	0.09	0.45	0.26	0.14	0.20	0.13
6.5	3.0	−0.11	0.02	0.34	0.06	0.78	0.03	0.09	0.46	0.28	0.14	0.21	0.12
7.5	3.4	−0.11	0.03	0.37	0.06	0.79	0.03	0.09	0.46	0.29	0.15	0.22	0.13
8.5	3.9	−0.11	0.03	0.39	0.07	0.8	0.04	0.09	0.47	0.29	0.15	0.22	0.13

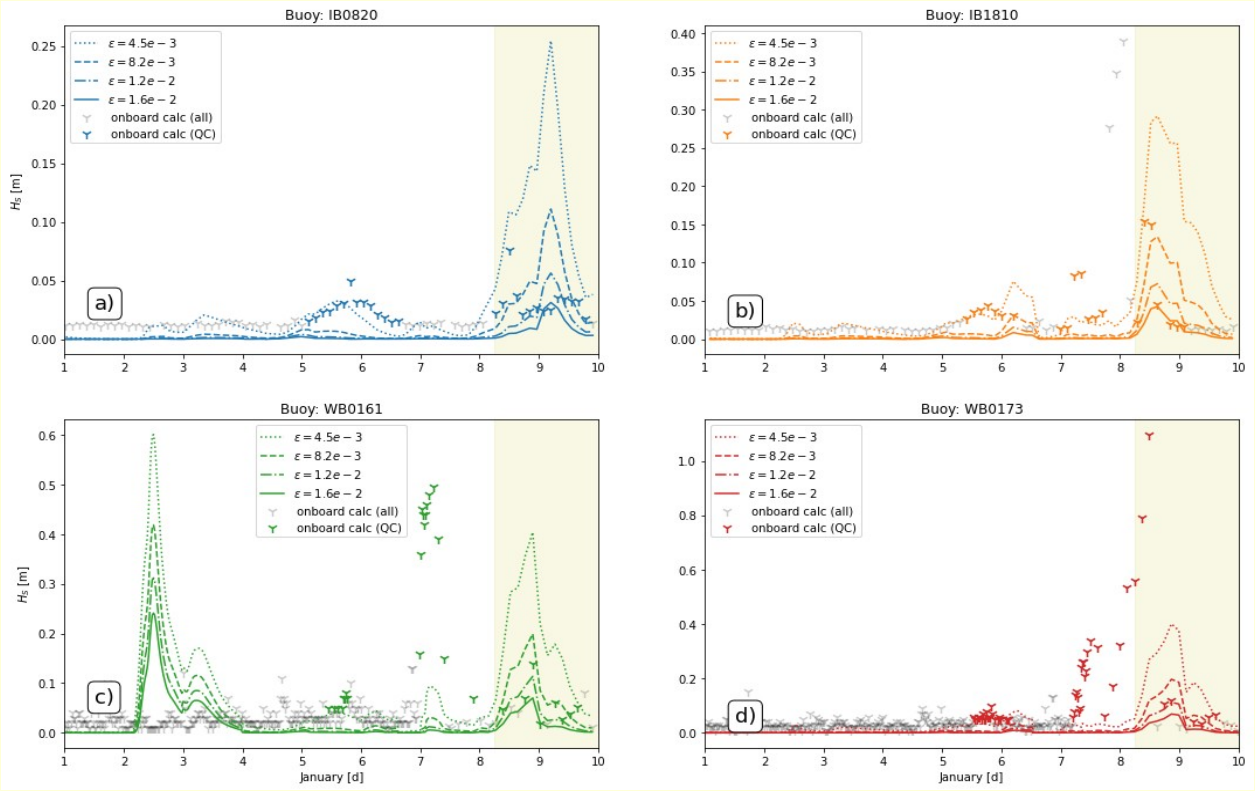

Figure 3.3. Modelled and observed H_S following the buoys. Model simulations shown for ϵ in [4.5e-3, 8.2e-3,1.2e-2,1.6e-2]. Coloured markers indicate quality controlled (QC) onboard buoy H_S observations. Gray markers indicate all onboard buoy H_S observations. The yellow highlighted area indicates the calibration period.

Our baseline simulation (C) captures the timing of wave events well, with peaks in H_S occurring at the same time as those observed by the buoys (Fig. 3.4). Its ability to accurately capture the magnitude of these peaks differs vastly between wave events, and sometimes even between different buoys for the same event. For the small wave activity on January 5, simulation C closely matches the observations for all buoys. For January 7, we see an increase in wave size at WB0161 and WB0173, but not IB0820 and IB1810. Simulation C well represents the wave activity of these latter two buoys, but under-represents the wave activity of the former two. For the large event on January 9, we see accurate representation for buoys IB1810 and WB0161, but a slight over-representation for IB0820, and a considerable under-representation for WB0173. For the observed peak on January 29, simulation C captures the wave activity at WB0161, but under-represents wave size at buoys IB1810 and WB0173. From January 29 on-wards, we observe a marked increase in

wave activity (this is due to a loss of sea ice to the north of the Davis Sea not shown here). For the large wave activity observed on February 1 to February 3, simulation C accurately captures the wave activity at IB1810 and WB0161 (apart from a brief under-representation on January 1). From February 5 to February 9, simulation C accurately follows the observations at buoy IB1810 with the exception of two short spikes (February 6, February 8). These short-lived spikes are due to model discretisation: the buoy is close to the border of the adjacent cell here (which is one cell less deep into the MIZ and therefore the waves here have been less heavily attenuated) and briefly enters it twice causing spikes in wave size tracking the buoy. There is then another peak in observed waves at IB1810 which simulation C under-represents (January 10), after which the simulation shows similar wave activity as observed by IB1810 (January 11 – 14).

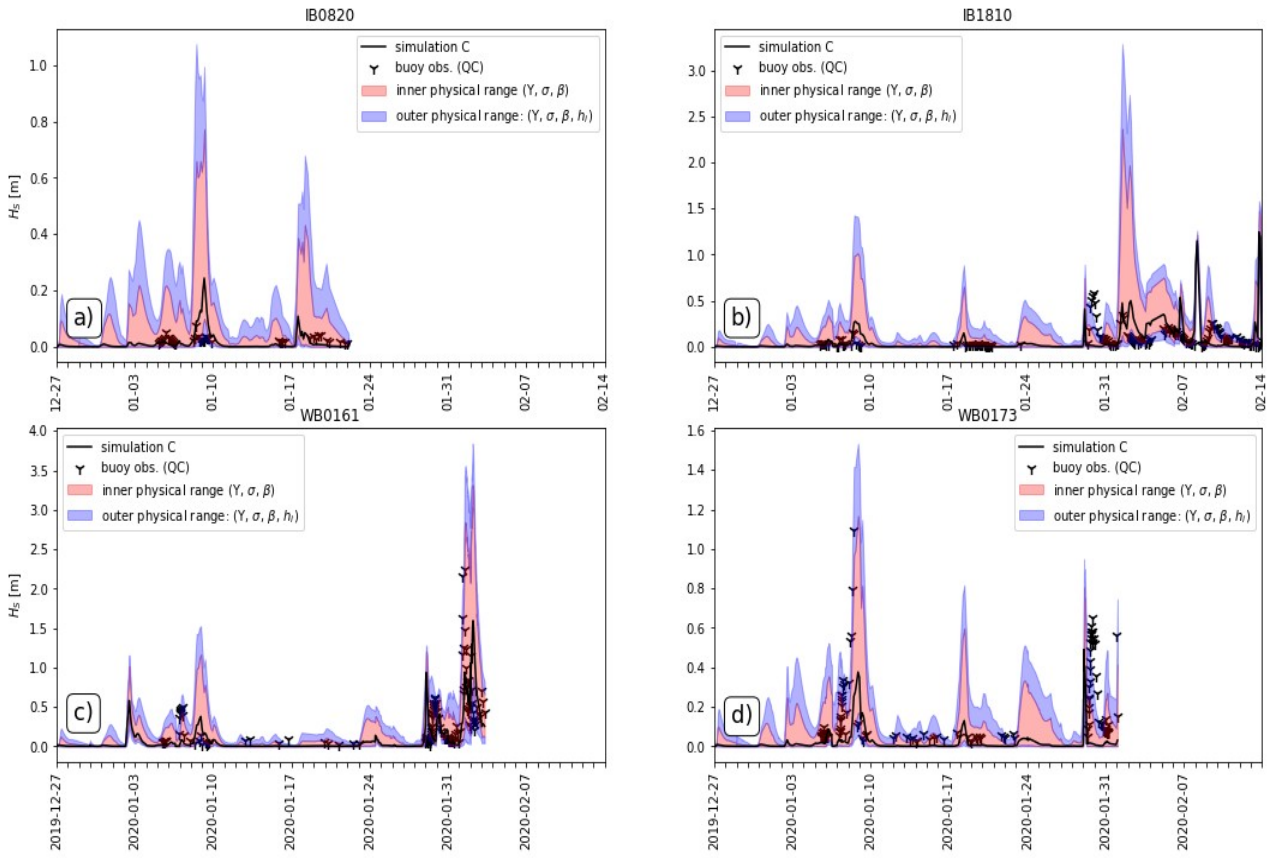

Figure 3.4. Modelled and observed H_S following the buoys. Black markers indicate quality controlled onboard buoy H_S calculations. The inner (outer) physical range is defined as the range between the inner (outer) upper and lower bounds (see table 3.2 for simulation details).

The difficulty for our baseline simulation (C) in consistently matching the observations is partly rooted in the highly heterogeneous nature of the ice field. The range in wave behaviour spanned by the additional simulations account for this heterogeneity (table 3.2). The H_S range spanned by our inner physical range (simulations B and D) captures the vast majority of observed H_S values. The H_S range spanned by our outer physical range (simulations A and E) captures the remainder, with one exception: January 29. The observations at buoys IB1810 and WB0173 on this day exceed the maximum of the outer physical range by approximately 0.1m (~20% of the peak). This is most likely due to weaker/thinner sea ice in the path from the ocean to the buoy than accounted for in the outer physical range. Note that this exceedance is not seen at the other buoy still active at this time

(WB0161). Figure 3.5 shows the energy-frequency spectrum for WB0173 on January 30 (modelled and observed). We see that simulation C captures the distribution of this energy very well, and that all observations fall entirely within the inner physical range. Thus, our results show confidence that the developed model can replicate the field observations within reasonable accuracy using the inner physical range.

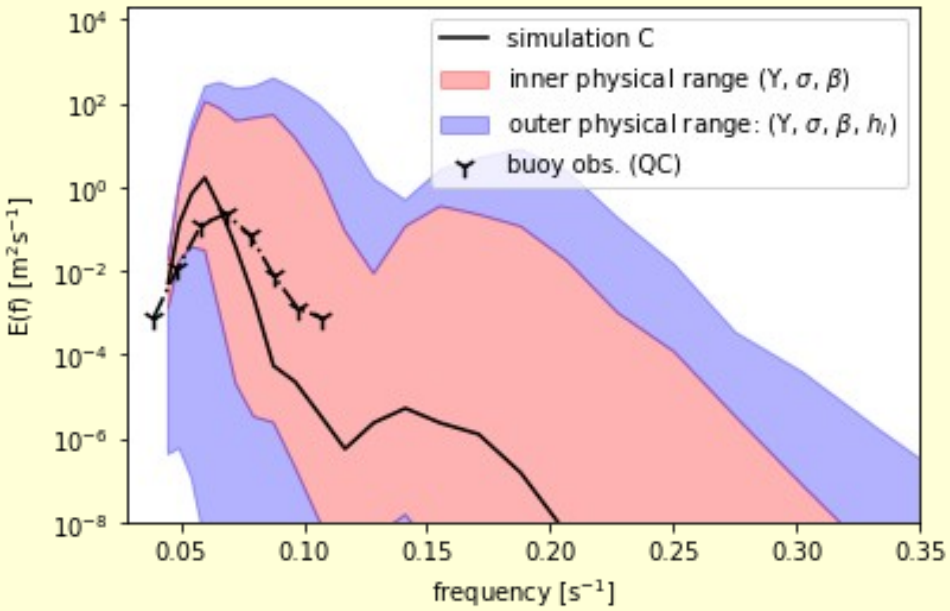

Figure 3.5. 1D modelled and observed wave spectra. Buoy observations shown by crosses. Buoy location for February 01 can be seen in figure 3.2. The inner (outer) physical range is defined as the range between the inner (outer) upper and lower bounds (see table 3.2 for simulation details). Buoy: WB0173; time: 2020-01-30T06:48.

3.3.1. Davis

Figure 3.6.a shows the number of grid points with unbroken ice in the Davis Sea throughout the study period (equivalent to total area coverage of unbroken ice), consisting of long periods of stability punctuated by short periods of rapid decline. Note that there are no increases in unbroken ice area due to the 'no refreeze' assumption. Recalling that the study period is characterised by sea ice retreat, this downwards trend in unbroken ice is logical. There is an inverse relationship between unbroken ice area and system stability, with the upper bounds (simulations D and E) showing more frequent and larger break-up than the lower (simulations A and B), which remain virtually constant, with approximately 20 cells of unbroken ice. Simulations D and E evolve from approximately 300 cells to just 40 by the end of the study period. This enhanced stability for the simulations A and B may be explained by a large barrier of broken ice (weakly attenuating the waves) shielding the unbroken ice from wave-induced break-up.

Figure 3.6.b-d shows the geographic distribution of the simulated unbroken ice for January 10, January 29 and February 11. Simulation D is the upper bound of the inner physical range. This simulated unbroken ice is superimposed on to images from the MODIS satellite for the corresponding days. The dates are selected to understand the spatial nature of the ice loss observed in Figure 3.6.a and to verify the simulated ice break-up. This verification relies on the MODIS satellite imagery (ModisSatIm) to differentiate between unbroken and broken ice. The MODIS satellite operates on the visible part of the electromagnetic spectrum, from which it can be difficult to determine features of the unbroken ice, such as sheet boundaries, unless bordered by ocean (the dark colour provides a strong contrast). Figure 3.6.c shows an example of a sheet boundary bordered by ocean, where the boundary between ocean and the land-fast sea ice is clearly visible in the ModisSatIm (F1 in Fig. 3.6). We assume that boundaries like this mark the extent of the unbroken ice. Simulation D shows unbroken ice extending to this edge (F2). We can also use the ModisSatIm to distinguish (e.g. F3).

The unbroken ice edge in simulation D has retreated by January 29, particularly on the north-west face of the sheet (F4), with this ice loss being attributed to the aforementioned January 23 break-up event (Fig. 3.6.a). The ModisSatIm corroborates this loss of unbroken ice in this region, with the ModisSatIm ice fragmented where before it was continuous (between F2 and F4). The unbroken ice in simulation D continues to follow the boundary of the ModisSatIm closely (F4), with the

exception of a slight high bias at 74.5°E, 69°S (F5). It is worth drawing to the reader's attention the 'unbroken' ice stretch at 74E, 69S (F6). This is not unbroken sea ice, but rather part of the ice shelf. This is a study focused on sea ice, and this shelf ice is therefore not represented within our model.

The unbroken ice in simulation D has retreated further by February 11, most evident at 75°E, 69.5°S (F7). The aforementioned high bias at 74.5°E, 69°S has disappeared. These ice losses can be attributed to the February 1 break-up event (Fig. 3.6.a). The ModisSatIm corroborates this loss of unbroken ice at 75°E, 69.5°S, with this part of the ocean now ice free (between F4 and F7). Again, the unbroken ice in simulation D follows the boundary of the ModisSatIm closely (F7).

Figure 3.6. (page opposite/following) a) Modelled number of unbroken ice grid points for the Davis Sea region. The inner (outer) physical range is defined as the range between the inner (outer) upper and lower bounds. See table 3.2 for simulation details. **b-d)** Model simulations of unbroken sea ice for the Davis Sea region. Blue dots mark modelled solid ice for the inner upper physical bound (simulation D; see table 3.2 for simulation details). Dashed and solid black contours mark lines of 15% and 85% sea ice concentration respectively. Buoy locations are shown by the coloured crosses. Corrected Reflectance satellite imagery from the MODIS satellites are shown (https://worldview.earthdata.nasa.gov). The colour of the 'F-numbers' refers to the lines of the same colour and are to be discussed in the text.

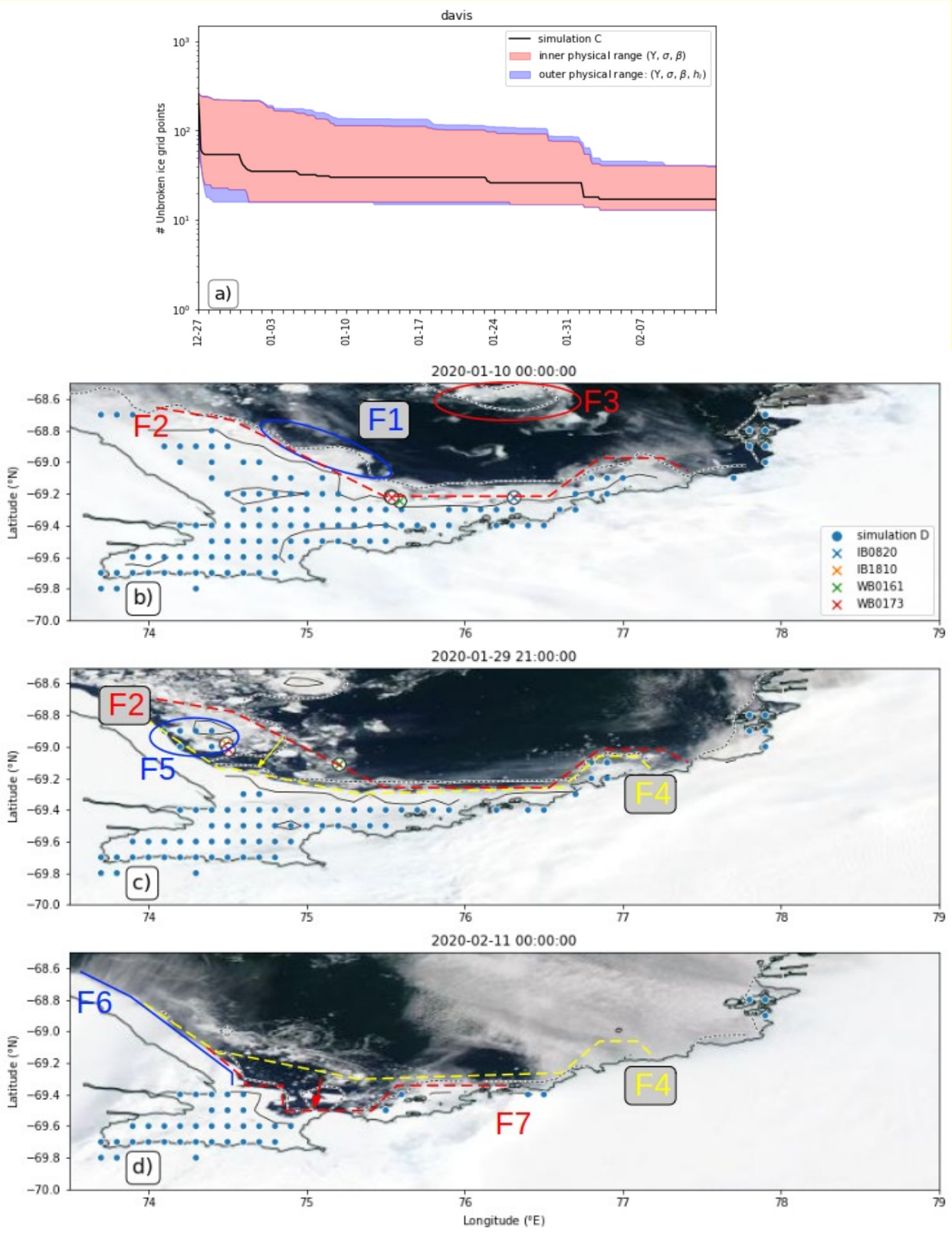
davis
simulation C
inner physical range (Y, σ, β)
outer physical range: (Y, σ, β, h_i)
Unbroken ice grid points
a)
12-27
01-03
01-10
01-17
01-24
01-31
02-07
2020-01-10 00:00:00
F1
F2
F3
simulation D
IB0820
IB1810
WB0161
WB0173
b)
2020-01-29 21:00:00
F2
F5
F4
c)
2020-02-11 00:00:00
F6
F4
F7
d)
Latitude (°N)
Longitude (°E)

3.3.2. Western and Central Sheets

The time series of the unbroken ice amount for the western and central sheets show similar features to that of the Davis Sea, namely prolonged periods of relative stability punctuated by short periods of rapid decline, and a greater stability for the lower bound simulations, with the upper bounds slowly converging towards them (Fig. 3.7.a-b). There is more unbroken ice in the western and central sheets relative to the Davis Sea, with the upper bounds beginning respectively at 1000 and 600 cells of unbroken ice, compared to the 300 of the Davis Sea. Note that the lower bounds for these regions consist of virtually no unbroken ice. For the central sheet, this happens instantly, whereas we see a few remnant cells of unbroken ice persist in the western sheet. The Davis Sea region was probably able to maintain more unbroken ice in the lower bound due to geographical (and ice field) wave protection. Also note that the ice loss in the central sheet consists of highly frequent but small break-up events, whilst it is less frequent but larger for the western sheet. This is also likely a due to protective difference resulting from a combination of the surrounding geography and ice field. The ice loss in the Davis Sea region is more similar to the western sheet in terms of frequency vs. magnitude.

Figure 3.7. (page opposite/following) a-b) Modelled number of unbroken ice grid points for the western and central sheets. The inner (outer) physical range is defined as the range between the inner (outer) upper and lower bounds. See table 3.2 for simulation details. **c-e)** Model simulations of unbroken sea ice for the western and central sheets. Blue and magenta dots mark modelled solid ice for the upper physical bounds (simulations D and E; see table 3.2 for simulation details). Dashed and solid black contours mark lines of 15% and 85% sea ice concentration respectively. Buoy locations are shown by the coloured crosses. Corrected Reflectance satellite imagery from the MODIS satellites are shown (https://worldview.earthdata.nasa.gov). The colour of the ‘F-numbers’ refers to the lines of the same colour and are to be discussed in the text.

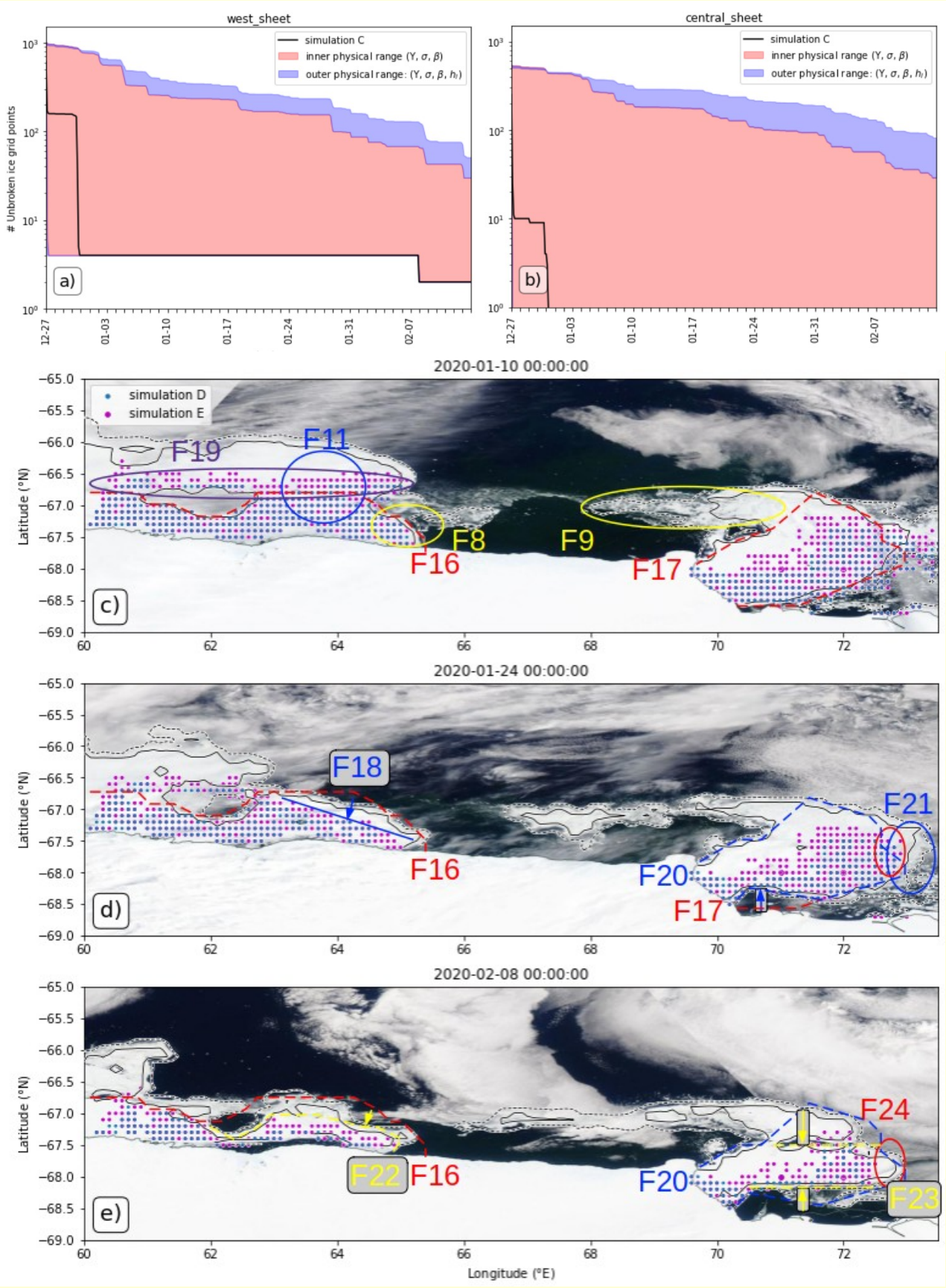
west_sheet
central_sheet
simulation C
inner physical range (Y, σ, β)
outer physical range: (Y, σ, β, hₜ)
Unbroken ice grid points
a)
b)
12-27
01-03
01-10
01-17
01-24
01-31
02-07
2020-01-10 00:00:00
simulation D
simulation E
F19
F11
F8
F16
F9
F17
c)
2020-01-24 00:00:00
F18
F16
F21
F20
F17
d)
2020-02-08 00:00:00
F22
F16
F24
F20
F23
e)
Latitude (°N)
Longitude (°E)

Figure 3.7.c-e shows the geographic distribution of the simulated unbroken ice for January 10, January 24 and February 8 (simulation D; the upper bound of the inner physical range) overlaid onto the ModisSatIm. The dates are slightly different to those of the Davis Sea analysis due to cloud cover interference. Beginning with January 10, we see a clear boundary in the ModisSatIm for much of the western and central ice sheets (e.g. F8). There is additional ice attached to these sheets which can be identified as broken ice (e.g. F9). It is somewhat ambiguous in some regions where the unbroken ice stops and the broken ice begins (e.g. F11). Here we use supplementary ModisSatIms to help determine the likely extent of the unbroken ice. In Figure 3.8, we highlight cracks/fragmentation in the ice that are not as clearly visible in Figure 3.7 for the western sheet (F12 and F13 in Fig. 3.8), allowing us to determine the likely extent of unbroken ice (F16 in Fig. 3.7). The unbroken ice in simulation D (the blue dots) follows this boundary from the ModisSatIm very well (F17). The central sheet appears to consist entirely of tightly packed broken ice (F14 in Fig. 3.8) with the exception of one large ice floe (which may be an ice berg calved from the ice shelf rather than being sea ice; F15). Note that this violates the initial assumption of the model that all sea ice is initially unbroken. The analysis of the central sheet will therefore proceed with the acknowledgement that this is tightly packed broken ice and not unbroken sea ice.

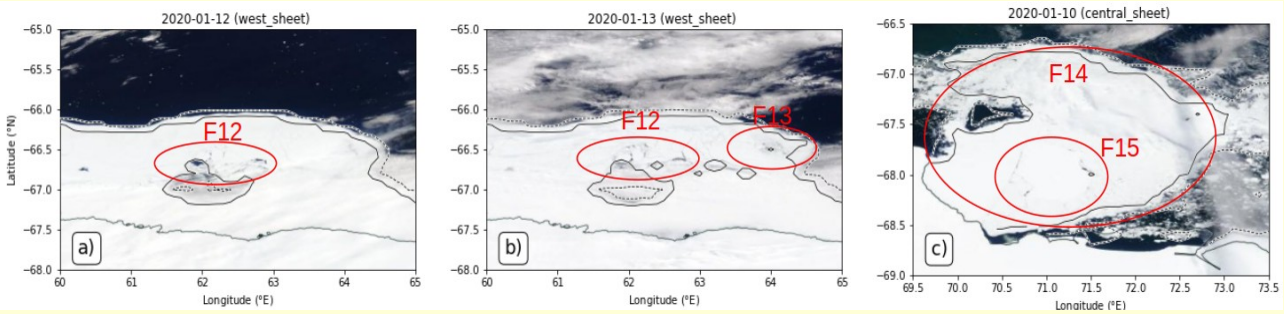

Figure 3.8. Corrected Reflectance satellite imagery from the Aqua and Terra MODIS satellites (https://worldview.earthdata.nasa.gov). Dashed and solid black contours mark lines of 15% and 85% sea ice concentration respectively. The colour of the 'F-numbers' refer to the lines of the same colour and are to be discussed in the text.

It is important to stress that the ice thickness used for the inner physical range simulations was only measured at the deployment site of the instruments (Davis Sea) and is therefore unlikely to be representative for the Western and Central Sheets. We therefore also show the results of simulation E in Figure 3.7 (unbroken ice market by the magenta dots), which considers an ice thickness double

that of simulation D. With respect to simulation C, an increased ice thickness increases the extent of unbroken ice for both the central and western sheets. This increase of unbroken ice present an interesting contradiction to the employed ice break-up threshold (Equation 3.3), which states that the ice break-up, I_{br}, increases with ice thickness. As ice thickness increases however, so too does attenuation (Equation 3.1), thereby decreasing the wave energy passing through the MIZ and subsequently available for the potential break-up of sea ice.

Although simulation D shows a significant contraction of the north eastern edge of the western ice sheet from January 10 to January 24 (F18), the unbroken ice in the ModisSatIm appears to maintain relatively stable over this period, essentially following the same contour as previously (F16; Fig. 3.7.d). This model ice loss (F18), largely occurring on January 18 (Fig. 3.7.a), has resulted in another low bias, now in the western sheet. Simulation E, with its thicker ice and reduced ice retreat, reduces this bias, but does result in a slight high bias in northerly extent of this ice sheet for January 10 however (F19), not yet registering the northern part of this sheet yet as broken. Considering that we used images from January 12 and 13 (Fig. 3.8.a-b) to diagnose the extent of the unbroken ice here (due to cloud cover), it is also possible that this ice in reality has not yet broken, and that the model is accurately representing the extent of unbroken ice here. We also see a retreat of the tightly packed broken ice in the central sheet on the southern border (ModisSatIm; F20). The model shows similar ice loss on the southern boundary, as well as additional ice loss on the eastern boundary (F21).

Over the next two weeks (January 24 - February 8), we see further contraction of the western sheet in both ModisSatIm and model (F22). By February 24, simulation E closely follows the ModisSatIm unbroken ice here, whilst simulation D maintains a low bias. The ModisSatIm shows significant losses incurred by the tightly packed broken ice in central sheet over this period. This consists of a large region detaching in the north, as well as some further losses to the southern boundary (Fig. 3.7.f; F23). Similar to the losses seen in the ModisSatIm (F23), the model shows ice retreat for the northern and southern boundaries, as well as some additional losses incurred to the eastern boundary (F24).

3.3.3. Polynya Barrier

The fourth region is the polynya barrier. For the time series of unbroken ice, we see the same model characteristic features as previously (Fig. 3.9.a): prolonged periods of relative stability punctuated by short, rapid declines, and greater stability for the lower bounds, with the upper bounds converging towards them. The lower bounds fall to zero cells of unbroken ice instantly; the upper bounds begin with 500-600. The ice loss here is more similar to the Davis Sea and western sheet in terms of frequency vs. magnitude of ice loss (less frequent, larger losses). Different here, however, is that all simulations have converged to zero unbroken ice by January 29, indicating very high confidence that the wave energy is sufficiently large to break all ice.

Figure 3.9.b-c shows the geographic distribution of the simulated unbroken ice for January 10 and January 24 (simulation D) overlaid onto the ModisSatIm. The ModisSatIm shows ice across the entirety of this region as broken. Simulation D, however, still shows some unbroken ice remaining here in the centre of the ice pack (F25). This unbroken ice is consumed by January 23 (Fig. 3.9.a,c).

Figure 3.9. (page opposite/following) a) Modelled number of unbroken ice grid points for the polynya barrier. The inner (outer) physical range is defined as the range between the inner (outer) upper and lower bounds. See table 3.2 for simulation details. **b-c)** Model simulations of unbroken sea ice for the polynya barrier. Blue dots mark modelled solid ice for the inner upper physical bound (simulation D; see table 3.2 for simulation details). Dashed and solid black contours mark lines of 15% and 85% sea ice concentration respectively. Buoy locations are shown by the coloured crosses. Corrected Reflectance satellite imagery from the MODIS satellites are shown (https://worldview.earthdata.nasa.gov). The colour of the ‘F-numbers’ refers to the lines of the same colour and are to be discussed in the text.

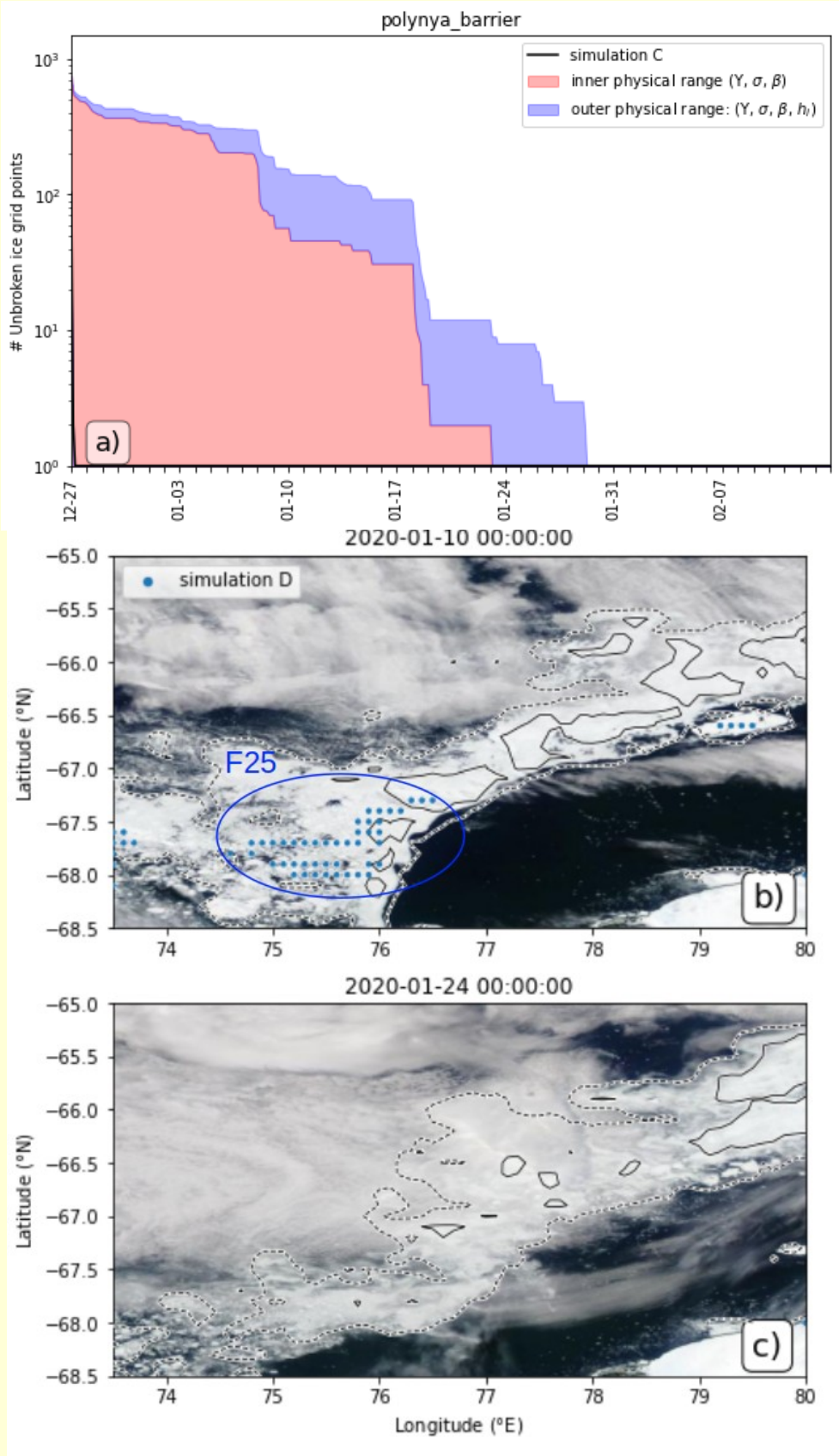
polynya_barrier
simulation C
inner physical range (Y, σ, β)
outer physical range: (Y, σ, β, h_i)
Unbroken ice grid points
10^3
10^2
10^1
10^0
a)
12-27
01-03
01-10
01-17
01-24
01-31
02-07
2020-01-10 00:00:00
simulation D
F25
b)
2020-01-24 00:00:00
c)
Latitude (°N)
−65.0
−65.5
−66.0
−66.5
−67.0
−67.5
−68.0
−68.5
74
75
76
77
78
79
80
Longitude (°E)

3.4. Discussion

Here we present a novel wave-sea ice interaction model applied to an Antarctic case study. We verify the model's performance firstly with respect to wave properties, and secondly with respect to the two-phase ice field (unbroken and broken). The model performs reasonably well in replicating the observations of waves in sea ice in the Davis Sea. Discrepancies between model and observations are largely caused by the highly spatial heterogeneous composition of the sea ice (i.e., Figs. 3.6-3.9). Specifically, the distance of the instruments to the landfast ice edge (and notably, the ice edge is adjacent to the polynya) is similar in magnitude as the grid resolution of the model, causing properties to vary greatly between neighbouring cells. This ultimately means that the calibration and validation of wave properties is very sensitive to the definition and discretisation of the model grid and model input, and the exact position at which the instrumentation is located with respect to the grid. The impact of the strong spatial variability of the ice cover can be observed in the model output and *in situ* observations in up to January 10, where the instruments are within close proximity of each other, nevertheless, present a substantially different significant wave height (Fig. 3.4). Given the major challenges in the modelling of waves in ice in this specific study, the comparison of the simulated wave field against the *in situ* observations is very positive (Figs. 3.4 and 3.5).

There are four assumptions made in this study which require some discussion with respect to their justification and/or implications: 1) ice thickness, strength and elasticity are homogeneous in space and time. While this is typical practice in the current state of the field due to difficulty of obtaining information of sea ice properties at vast scales, it is a limitation which hinders the reliability of the simulation across large geophysical scales and long time duration. We see a substantial difference in results for both wave attenuation and ice break-up when the complete physical range of the ice properties are considered; 2) sea ice cannot transition from its 'broken' state to a 'unbroken' state (i.e. no refreezing is allowed). We consider this a reasonable assumption considering the season of the simulations but note that such assumption is likely invalid when temperatures become lower; 3) unbroken ice is geographically anchored (i.e. does not drift). The unbroken sea ice identified by our model appears to be primarily land-fast sea ice and, according to the ModisSatIm, does not appear to be drifting. The unbroken sea ice in the polynya barrier, however, is not land-fast, but breaks up so rapidly that this is not a concern; 4) dissipation is the dominant mechanism for attenuation of

waves in ice. This is a valid assumption for the long waves characteristic of this region, but may be invalid where shorter waves are more dominant (e.g. the Arctic) as scattering may dominate (Wadhams et al., 1986; Sutherland & Gascard, 2016).

We believe this model to be of general interest to the field of wave-sea ice interaction for the following reasons: 1) the threshold used here for sea ice break-up was developed across a diverse variety of ice scales, meaning that the model is not limited to a specific location/scale, 2) the attenuation model within our model can effectively be considered a generic dissipative model with a power-4 frequency dependence ($k \sim f^2$) and a single calibration coefficient, meaning we are not carrying any assumptions about the dominant relevant physical attenuative processes (apart from attenuation following a power-4 frequency dependence in fitting with the range reported by Rogers et al., 2021).

There is no straightforward method available to validate the simulated two-phase ice field and we had to resort to visual analysis using MODIS satellite imagery. Despite the subjectivity of this approach and the simplicity and limitations of the model, the performance of our model in identifying regions of broken and unbroken ice is satisfactory. A major source of error between the simulations and the observations is that the wave-ice coupled model only considers break-up induced by waves while other processes, including wind and currents, have the capacity to break the ice as well. Aside from the uncertainty in sea ice material and physical properties, the exclusion of these break-up mechanisms can, in part, explain why sections of the sea ice are considered unbroken by the model, but appear as broken in the satellite images. Additionally, parts of the ice cover may have been broken prior to the study period, and remain so, potentially causing a bias later in the simulations if the waves are not strong enough to break this ice at a later stage in the simulation. We see this bias manifestation for the central sheet, where there remains a considerable amount of unbroken ice in the model, despite the region consisting of broken ice from the beginning (as shown by the ModisSatIm). The polynya barrier region shows the opposite case: despite the discrepancy between the model assumption (all ice initially unbroken) and reality (all sea ice broken as shown by the ModisSatIm), the model is able to provide a realistic representation of sea ice for the study period.

The strong correspondence between the simulated two-phase ice cover and satellite imagery substantiates the capacity of waves to influence the sea ice morphology in the MIZ and at very short time scales. This identifies the importance of two-way coupling of waves and sea ice for accurate prediction in forecasting models. Further studies are, however, required to assess model performance at different sites, preferably at sites where more details are available on the mechanical properties of the ice and ice thickness.

3.5. Conclusions

This study presents a new simple wave-sea ice coupled model, and applies it to a case study in the Antarctic over the summer of 2019/2020. Our model can be summarised as follows: 1) sea ice takes a binary form, either 'broken' or 'unbroken', 2) waves can break sea ice, transitioning it from unbroken to broken, 3) the threshold of Voermans et al. (2020) is used to identify when this occurs, 4) there are two modes of attenuation for waves in ice (dependent upon the ice state), representing the on/off attenuation reported in Collins et al. (2015) and Ardhuin et al. (2020), 5) through the attenuation and ice break-up described above, we achieve two-way wave-sea ice coupling, thereby allowing wave-sea ice feedbacks. We note here that this study is the first to implement observation-based features 3) and 4) within a numerical wave model. We use *in situ* buoy observations to validate the modelled waves, and satellite imagery to validate the modelled sea ice. The model is run for a variety of ice properties to understand the range of possible physical behaviour of the system.

The baseline simulation (C) captures the timing of wave events but, due to the spatial heterogeneity of the ice field, has some trouble in accurately capturing the magnitude of the waves at each buoy. We account for this spatial heterogeneity here by varying the mechanical properties of the ice within a likely physical range, allowing us to capture the full range of wave behaviour observed by the buoys. This accuracy of the model holds true not just for significant wave height, but also for the spectral distribution of wave energy.

We note an inverse relationship between quantity of unbroken ice and system stability, with systems with more ice being prone to more frequent and larger break-up events. This is likely due to the shielding afforded to the unbroken ice by the broken ice surrounding. Using satellite imagery for verification, we also demonstrate the model's high ability to represent sea ice break-up (and consequently the two-phase sea ice field), accurate in both the spatial and temporal dimensions. The accuracy of this model also substantiates the ability of the observation-based features of a binary sea ice state (unbroken/broken) with associated on/off attenuation (model feature 4), and a non-dimensional threshold which determines when the ice transitions from unbroken to broken (model feature 3).

Lastly, we stress the importance of accurately representing the state of the sea ice. Sea ice forms a crucial barrier between air and sea, and understanding when and how it breaks is crucial to understanding polar regions. As we do not allow for break-up by other mechanisms in this study (e.g. wind or currents), the sea ice break-up here is solely due to the waves. The ability of our model to accurately represent this sea ice break-up thereby substantiates that waves have a critical influence on the morphology of the MIZ, and at very short time scales too.

3.6. References

Ardhuin, F., Otero, M., Merrifield, S., Grouazel, A., & Terrill, E. (2020). Ice Breakup Controls Dissipation of Wind Waves Across Southern Ocean Sea Ice. *Geophysical Research Letters*, *47*(13), 1–7. https://doi.org/10.1029/2020GL087699

Bateson, A.W., Feltham, D.L., Schröder, D., Hosekova, L., Ridley, J.K., & Aksenov, Y. (2020). Impact of sea ice floe size distribution on seasonal fragmentation and melt of Arctic sea ice. *Cryosphere, 14, 403–428.*

Beitsch, A., Kaleschke, L. and Kern, S. (2013). "AMSR2 ASI 3.125 km Sea Ice Concentration Data, V0.1", Institute of Oceanography, University of Hamburg, Germany, digital media

Boutin, G., Lique, C., Ardhuin, F., Rousset, C., Talandier, C., Accensi, M., & Girard-Ardhuin, F. (2020). Towards a coupled model to investigate wave-sea ice interactions in the Arctic marginal ice zone. *Cryosphere*, *14*(2), 709–735. https://doi.org/10.5194/tc-14-709-2020

Collins, C. O., Rogers, W. E., Marchenko, A., & Babanin, A. V. (2015). In situ measurements of an energetic wave event in the Arctic marginal ice zone. *Geophysical Research Letters*, *42*, 1–8. https://doi.org/10.1002/2015GL063063

Curry, J.A., Schramm, J.L., & Ebert, E.E. (1995). Sea Ice-Albedo Climate Feedback Mechanism. *J. Clim., 8, 240–247.*

Feltham, D. L. (2005). Granular flow in the marginal ice zone. *Philosophical Transactions of the Royal Society of London A: Mathematical, Physical and Engineering Sciences*, *363*, 1677–1700.

Hasselmann, K., Barnett, T.P., Bouws, E., Carlson, H., Cartwright, D.E., Enke, K., Ewing, J.A., Gienapp, H., Hasselmann, D.E., Kruseman, P., Meerburg, A., Müller, P., Olbers, D.J., Richter, K., Sell, W., & Walden, H. (1973). Measurements of wind-wave growth and swell decay during the Joint North Sea Wave Project (JONSWAP), Dtsch. Hydrogr. Z. Suppl. A 8(12), 95p.

Karulina, M., Marchenko, A., Karulin, E., Sodhi, D., Sakharov, A., & Chistyakov, P. (2019). Full-scale flexural strength of sea ice and freshwater ice in Spitsbergen Fjords and North-West Barents Sea. *Appl. Ocean Res.,* 90, 101853. https://doi.org/10.1016/j.apor.2019.101853

Kohout, A. L., & Meylan, M. H. (2008). An elastic plate model for wave attenuation and ice floe breaking in the marginal ice zone. *Journal of Geophysical Research: Oceans*, *113*(C9).

Langhorne, P. J., Squire, V. A., Fox, C., & Haskell, T. G. (1998). Break-up of sea ice by ocean waves. *Annals of Glaciology*, *27*, 438–442.

Li, J., Babanin, A.V., Liu, Q., Voermans, J.J., Heil, P., & Tang, Y. (2021). Effects of Wave-Induced Sea Ice Break-Up and Mixing in a High-Resolution Coupled Ice-Ocean Model. *J. Mar. Sci. Eng.*, 9, 365. https://doi.org/10.3390/jmse9040365

Liu, Q., W. E. Rogers, A. V. Babanin, I. R. Young, L. Romero, S. Zieger, F. Qiao, and C. Guan, 2019: Observation-based source terms in the third-generation wave model wavewatch III: Updates and verification. J. Phys. Oceanogr., 49, 489–517, https://doi.org/10.1175/JPO-D-18-0137.1.

Liu, Q., Babanin, A. V., Rogers, W. E., Zieger, S., Young, I. R., Bidlot, J., Durrant, T., Ewans, K., Guan, C., Kirezci, C., Lemos, G., MacHutchon, K., Moon, I., Rapizo, H., Ribal, A., Semedo, A., & Wang, J. (2021). Global Wave Hindcasts Using the Observation-Based Source Terms: Description and Validation. *Journal of Advances in Modeling Earth Systems*, *13*(8), 1–38. https://doi.org/10.1029/2021ms002493

Longuet-Higgins, M. S. (1977). The mean forces exerted by waves on floating or submerged bodies with applications to sand bars and wave power machines. *Proceedings of the Royal Society of London A: Mathematical, Physical and Engineering Sciences*, *352*, 463–480.

Longuet-Higgins, M. S., & Stewart, R. W. (1962). Radiation stresses and mass transport in surface gravity waves with application to 'surf beats.' *Journal of Fluid Mechanics*, *13*, 481–504.

McPhee, M. G. (1980). An analysis of pack ice drift in summer. *Sea Ice Processes and Models*, 62–75.

Montiel, F., Squire, V. A. & Bennetts, L. G. (2016). Attenuation and directional spreading of ocean wave spectra in the marginal ice zone. *J. Fluid Mech.*, *790*, 492–522, https://doi.org/10.1017/jfm.2016.21.

Montiel, F., Squire, V. A., Doble, M., Thomson, J., & Wadhams, P. (2018). Attenuation and Directional Spreading of Ocean Waves During a Storm Event in the Autumn Beaufort Sea Marginal Ice Zone. *Journal of Geophysical Research: Oceans*, *123*(8), 5912–5932. https://doi.org/10.1029/2018JC013763

Rabault, J., Sutherland, G., Gundersen, O., Jensen, A., Christensen, K. H., Marchenko, A., & Breivik, Ø. (2020). An open source, versatile, affordable waves in ice instrument for scientific measurements in the polar regions. *Cold Regions Science and Technology*, *170*(102955).

Rogers, W. E., Meylan, M. H., & Kohout, A. L. (2021). Estimates of spectral wave attenuation in Antarctic sea ice, using model/data inversion. *Cold Regions Science and Technology*, *182*(June 2020), 103198. https://doi.org/10.1016/j.coldregions.2020.103198

Scientific Committee on Antarctic Research. (2000). Antarctic Digital Database, Version 3.0. Database, manual and bibliography. *Antarctic Digital Database Consortium*.

Shen, H. H., & Ackley, S. (1991). A one-dimensional model for wave-induced ice-floe collisions. *Annals of Glaciology*, *15*, 87–95.

Squire, V. A. (2020). Ocean Wave Interactions with Sea Ice: A Reappraisal. *Annual Review of Fluid Mechanics*, *52*, 37–60. https://doi.org/10.1146/annurev-fluid-010719-060301

Sutherland, P., & Gascard, J.-C. (2016). Airborne remote sensing of ocean wave directional wavenumber spectra in the marginal ice zone. *Geophysical Research Letters*, 43, 5151–5159, doi:10.1002/2016GL067713.

Steele, M.: Sea Ice Melting and Floe Geometry in a Simple Ice-Ocean Model, J. Geophys. Res., 97, 17729–17738, 1992.

Stopa, J. E., Sutherland, P., & Ardhuin, F. (2018). Strong and highly variable push of ocean waves on Southern Ocean sea ice. *Proceedings of the National Academy of Sciences*, *115*, 5861–5865.

Sutherland, G., Rabault, J., Christensen, K. H., & Jensen, A. (2019). A two layer model for wave dissipation in sea ice. *Applied Ocean Research*, *88*(October 2018), 111–118. https://doi.org/10.1016/j.apor.2019.03.023

The WAVEWATCH III Development Group (WW3DG). (2019). User manual and system documentation of WAVEWATCH III version 6.07. *NOAA / NWS / NCEP / MMAB Technical Note*, *333*.

Thomson, J., & Rogers, W. E. (2014). Swell and sea in the emerging Arctic Ocean. *Geophysical Research Letters*, *41*, 3136–3140.

Timco, G. & Weeks, W. (2010). A review of the engineering properties of sea ice. *Cold Reg. Sci. Technol.,* 60, 107–129.

Toffoli, A., Bennetts, L. G., Meylan, M. H., Cavaliere, C., Alberello, A., Elsnab, J., & Monty, J. P. (2015). Sea ice floes dissipate the energy of steep ocean waves. *Geophysical Research Letters*, *42*(20).

Voermans, J. J., Babanin, A. V., Thomson, J., Smith, M. M., & Shen, H. H. (2019). Wave Attenuation by Sea Ice Turbulence. *Geophysical Research Letters*, *46*(12), 6796–6803. https://doi.org/10.1029/2019GL082945

Voermans, J. J., Rabault, J., Filchuk, K., Ryzhov, I., Heil, P., Marchenko, A., Collins, C. O., Dabboor, M., Sutherland, G., & Babanin, A. V. (2020). Experimental evidence for a universal threshold characterizing wave-induced sea ice break-up. *Cryosphere*, *14*(11), 4265–4278. https://doi.org/10.5194/tc-14-4265-2020

Voermans, J. J., Liu, Q., Marchenko, A., Rabault, J., Filchuk, K., Ryzhov, I., Heil, P., Waseda, T., Nose, T., Kodaira, T., Li, J., & Babanin, A. V. (2021). Wave dispersion and dissipation in

landfast ice: comparison of observations against models. *Cryosphere, 15,* 5557-5575. https://doi.org/10.5194/tc-15-5557-2021

Wadhams, P., Squire, V. A., Ewing, J. A., & Pascal, R. W. (1986). The effect of the marginal ice zone on the directional wave spectrum of the ocean. *Journal of Physical Oceanography*, *16*, 358–376.

Wessel, P., & Smith, W. H. F. (1996). A global, self-consistent, hierarchical, high-resolution shoreline database. *Journal of Geophysical Research*, *101*(B4), 8741–8743. https://doi.org/https://doi.org/10.1029/96JB00104

Williams, T. D., Rampal, P., & Bouillon, S. (2017). Wave-ice interactions in the neXtSIM sea-ice model. *The Cryosphere Discussions*, 1–28.

This page intentionally left blank.

This page intentionally left blank.

Chapter 4:
Wave-Orbital Induced Turbulence: a Vital Source of Mixing within the Ocean

Waves are more than just an ocean surface phenomenon. Waves induce orbital motion of the water particles that extends to depths of more than 100m. This wave-orbit can stretch and amplify turbulent vortices within the ocean and impart energy to them (known as the Benilov instability mechanism). This loss of energy means attenuation of the waves, and is an important aspect of the BYDBR observation-based wave physics. This deposition of wave energy into the ocean however is routinely neglected by the ocean modelling communities. Its impact is far from negligible however, leading to additional mixing to depths of more than 100m and substantial flow on effects for oceanic heat and salinity fluxes. This is real physics that the ocean models are missing, the inclusion of which is likely to aid our understanding and prediction of the ocean. Here we incorporate this additional mixing into the the NEMO ocean model and study its effects.

4.1. Introduction

Surface waves play a key role in heat and other exchanges at the atmosphere-ocean interface (Cavaleri et al., 2012). Among these, waves can modify vertical mixing processes through providing additional turbulence in the upper layers of the ocean, for example the turbulence injection associated with breaking waves, a critical source of mixing within this layer (Kukulka & Brunner, 2015). These waves can also generate turbulence in the ocean without breaking. With a depth scale the same as the wavelength (order 100m in open ocean; Babanin, 2006), this wave-turbulence source penetrates much deeper than that related to breaking and enables mixing throughout (Babanin and Haus, 2009) and deepening of the mixed layer (Babanin et al., 2009). There are several mechanisms for such wave-turbulence production, the most general two perhaps being the enhancement (instability) of pre-existing three-dimensional turbulence to the wave orbital motion (Benilov, 2012) and Langmuir turbulence (McWilliams et al., 1997). The former, known as the Benilov mechanism, relies on wave orbital motion imparting energy to the turbulence through the stretching of vortex lines. The Langmuir turbulence is the fully turbulent flow associated with Langmuir circulation. Both proposed mechanisms predict that the intensity of wave-induced turbulence increase with wave height. Turbulence by wave-orbital motion is widely recognized as important, and as such has been represented recently in many numerical ocean models. Representations of the wave-orbital induced turbulence have been able to improve model accuracy (Huang et al, 2012; Qiao et al., 2004; Shu et al., 2011; Song et al., 2011) and demonstrate the ability of this mechanism to facilitate turbulence related phenomena such as sediment suspension (Pleskachevsky et al., 2011), hurricane mixing through the thermocline (Toffoli et al., 2012), and swell decay (Young et al., 2013). The parameterisation of Ghantous and Babanin (2014) offers a direct representation of the turbulent kinetic energy (TKE) production by non-linear interactions of wave orbital motion with turbulence vortices. This parameterisation is based on theory and evidence from a variety of sub-disciplines: consistent and redundant dimensional (Babanin, 2009; Bowden, 1950), experimental (Babanin and Haus, 2009), numerical (Babanin and Chalikov, 2012), and observational (Young et al., 2013). Inclusion of this parameterisation within global ocean models has been demonstrated to reduce biases in mixed layer depth (Walsh et al., 2017), increase accuracy of global SST (Stoney et al., 2018) and increase accuracy in seasonal amplitude of the extent of Antarctic sea ice (Thomas et al., 2019).

One model that may benefit from such a proper treatment of wave-orbital induced turbulence is NEMO (Madec & The NEMO Team, 2019). NEMO suffers from a too-shallow mixed layer depth (MLD) bias, and consequently a too-hot summer SST bias in the Southern Ocean. This issue is currently addressed with the *ad hoc* parameterisation of Rodgers et al. (2014), which acts to dramatically enhance mixing in storm belts, particularly in the Southern Ocean. Rodgers et al. (2014; hereafter REA14) superimposes an additional TKE profile that decays exponentially with depth within the existing vertical TKE scheme.

$$S=(1-f_i)f_r e_s e^{-z/h_\tau} \qquad (4.1)$$

where e_s is the surface boundary condition, f_i is the ice fraction, f_r is the penetrative fraction of TKE into the ocean, z is depth and h_τ is the vertical mixing length scale. The vertical mixing length scale is prescribed as a function of latitude, with h_τ ranging from 0.5m around the equator to a maximum of 30m in the high-latitudes.

$$h_\tau=\max(0.5,\ \min(30\ ,\ 45*\sin\theta)) \qquad (4.2)$$

There are multiple versions of this available within NEMO; this is the version used here and it differs slightly to the original form of REA14. This function is optimised to counter the pre-existing mixed layer bias in an empirical manner. The need for such a parameterisation indicates that NEMO is missing some key physics. We hypothesise that this missing physics is wave-orbital induced turbulence, which would mean a direct parameterisation for this phenomenon would be much more suited to address NEMO's MLD shallow bias. To test this hypothesis we implement and test Ghantous and Babanin's (2014) parameterisation for wave-orbital induced turbulence into NEMO.

4.2. Methods

NEMO is run on a tripolar ORCA 1.0° grid configuration with 75 vertical levels. The uppermost level is 1 metre thick. The model is actively coupled to NEMO's sea ice model, SI^3 (Aksenov et al., 2019), and is relaxed weakly toward a climatology in temperature (3 year e-folding time). No SST relaxation is performed. At ECMWF, NEMO can be coupled to the atmospheric model with wave forcing from the wave model. However, here we use the forced (ocean-only) integration of NEMO using hourly forcing from the ERA5 reanalysis (Hersbach et al., 2020). ERA5 is a continuously updated atmospheric and wave field reanalysis which began in 1979 at the time when the simulations were ran, but which now extends back to 1959. The resolution of the ERA5 wave model is 0.36° on the equator but the resolution is kept approximately constant globally through the use of a quasi-regular latitude-longitude grid where grid points are progressively removed toward the poles (Janssen, 2004). Similarly, the atmospheric model fields are archived on a reduced Gaussian grid (TL 639) of approximately 0.25° resolution at the equator. The model hindcast is run over the period 1979 - 2012. This information is summarised in table 4.1. The results here are based on the NEMO4.01 configuration that existed in May, 2020. The configuration of NEMO4.01 is still evolving however, meaning that these results are to be seen only as preliminary results.

NEMO uses a turbulence closure model, in which the time evolution of TKE is described by

$$\frac{\partial \bar{e}}{\partial t} = \frac{K_m}{e_3^2}\left[\left(\frac{\partial u}{\partial z}\right)^2+\left(\frac{\partial v}{\partial z}\right)^2\right] - K_\rho N^2 + \frac{1}{e_3}\frac{\partial}{\partial z}\left[\frac{A^{vm}}{e_3}\frac{\partial \bar{e}}{\partial z}\right] - c_\epsilon\frac{\bar{e}^{3/2}}{l_\epsilon} \qquad (4.3)$$

The time evolution of TKE is governed by four processes: the production of TKE through vertical shear, its destruction through stratification, its vertical diffusion and its Kolmogorov-type dissipation (Kolmogorov, 1942). We can then account for the production of TKE due wave-orbital motion through the inclusion of an additional term

$$\frac{\partial \bar{e}}{\partial t} = \frac{K_m}{e_3^2}\left[\left(\frac{\partial u}{\partial z}\right)^2+\left(\frac{\partial v}{\partial z}\right)^2\right] - K_\rho N^2 + \frac{1}{e_3}\frac{\partial}{\partial z}\left[\frac{A^{vm}}{e_3}\frac{\partial \bar{e}}{\partial z}\right] - c_\epsilon\frac{\bar{e}^{3/2}}{l_\epsilon} + P_{\text{wom}} \qquad (4.4)$$

where P_{wom} is the production due to wave-orbital motion and is represented according to the parameterisation of Ghantous and Babanin (2014),

$$P_{\text{wom}}(z) = b_1 k \left(\frac{\omega_p H_S}{2} e^{-kz}\right)^3 \qquad (4.5)$$

where b_1 is an empirical constant set to 0.0014 following Young et al. (2013), k is wavenumber, ω_p is peak angular frequency and H_S is significant wave height. Upon incorporation into NEMO we found that this parameterisation resulted in too vigorous mixing. As such we reduced the parameter b_1 from b_1=1.4*10^{-3} to b_1=0.7*10^{-4}. This value provided best overall performance with respect to SST and potential temperature (the temperature the water would have when brought adiabatically to the surface - a more informative parameter than temperature when dealing with the vertical). Wave breaking here is represented as in Breivik et al. (2014) in which the TKE from the breaking waves is a surface flux, prescribed as a Dirichlet boundary condition. In the ERA5 re-analysis there is high uncertainty with regards to waves in the marginal ice zone (ice concentration over 30%). As such, we can't rely on wave-based parameterisations for oceanic mixing and have to continue to use the REA14 parameterisation for this region. The first experiment is run with the model as detailed above. We also run a second 'control' experiment for comparison. The control uses the REA14 parameterisation and no representation of wave-orbital induced turbulence (i.e. the operational default; see table 4.2).

We assess the performance of each run against climatological observed MLD from the Argo campaign[5] (obtained from http://mixedlayer.ucsd.edu/), observations of SST from the ESACCI satellite, and potential temperature (θ) as given by the ERA5 reanalysis.

5 The climatological Argo data is for the 2000-2018 period, whereas the analysis is run from 1979 - 2012. This is acceptable considering the change in MLD climatology over this period is negligible (analysis not shown here).

Table 4.1. NEMO ocean model settings.

Grid	ORCA1_Z75
Horizontal resolution	ORCA 1.0°
Vertical resolution	75 levels (1m at the surface)
Simulation period	1979 – 2012
Atmospheric forcing	ERA5
Wave forcing	ERA5
Data assimilation	OFF
SST damping	OFF
3D damping to climate	ON (3 year Newtonian relaxation)
Ice model	SI[3]

Table 4.2. NEMO ocean hindcast simulations. REA14 refers to the Rodgers et al. (2014) *ad hoc* mixing.

GRID	**wave-orbital induced turbulence**	**REA14**
CONTROL (hdys)	NO	YES
WO_MIXING (heea)	YES (except in MIZ)	NO (except in MIZ)

This page intentionally left blank.

4.3. Results

Relative to the CONTROL simulation, the WO_MIXING simulation shows mixed layer deepening for almost all regions in DJF (Fig. 4.1). This is most pronounced in the storm belts. We also see a confined but considerable shallowing in the North Atlantic at 60°N. The JJA months show a very different pattern, with a considerable shallowing of the mixed layer all regions south of 30°S. The magnitude of this shallowing is approximately 2 times larger than the changes seen in the DJF months (~20m compared to ~10m).

To gain an insight into the seasonal cycle of MLD, we select two regions with differing MLD characteristics: the Southern Ocean and North Pacific. The Southern Ocean is particularly important as it is the region in which NEMO (and ocean models more generally) typically struggle to accurately represent mixing. The North Pacific area average presents a simple case of year-round deepening of the mixed layer in the WO_MIXING simulation (Fig. 4.2). The Southern Ocean is more interesting with a deepening of the mixed layer in Austral summer (DJF), yet shallowing throughout the rest of the year. This translates to a reduction in the amplitude of the MLD seasonal cycle. These changes improve biases in MLD relative to the Argo observations for both regions, but particularly for the Southern Ocean.

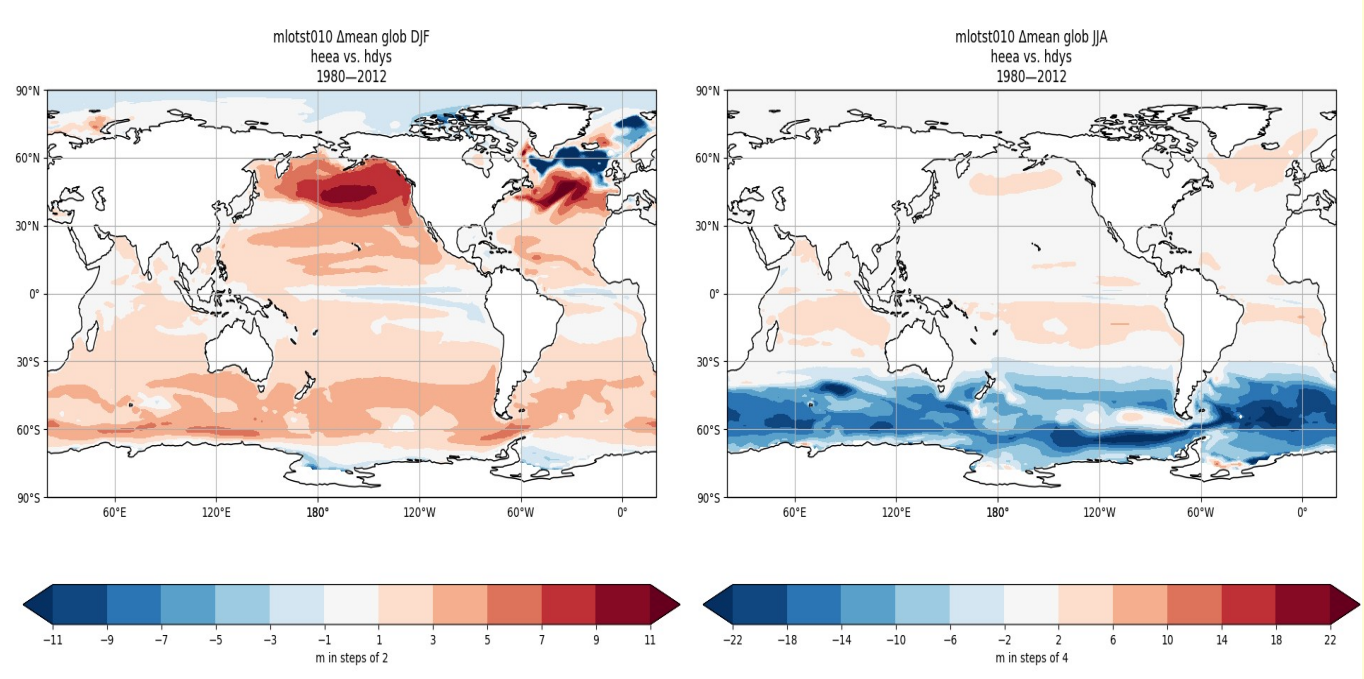

Figure 4.1. Mean difference in mixed layer depth between the WO_MIXING and CONTROL simulations for the months DJF (left) and JJA (right) for the years 1980-2012.

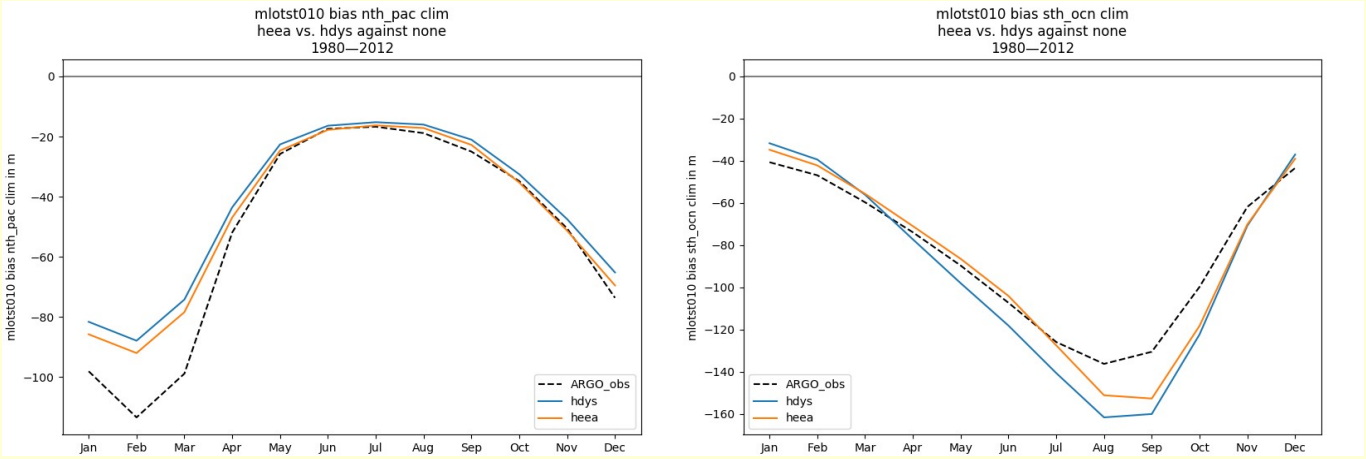

Figure 4.2. Mixed layer depth climatology for the North Pacific (left; 30-60°N; 120°E-120°W) and Southern Ocean (right; 30-90°N; all longitudes) for the WO_MIXING and CONTROL simulations for the years 1980-2012. Argo data for the period 2000-2018 is also shown.

These changes in mixing also have considerable influence on heat fluxes and therefore SST. We see widespread increases in SST across the mid- to high- latitudes for DJF relative to the control, and decreases in some equatorial regions (Fig. 4.3). For JJA this signal is reversed, with widespread decreases in SST in the mid- to high- latitudes, and increases in equatorial regions.

The effect on model performance for SST in DJF appears more or less neutral (Fig. 4.4), with approximately equal areas of model degradation and improvement (respective increases and decreases in RMSE). JJA however is dominated by considerable model degradation in the high latitudes of the North Pacific and North Atlantic (increases upwards of 0.25 K). Presenting this information in a globally averaged way, we see that the biases are reduced for the months December to April in the WO_MIXING simulation, but increased for May to November (Fig. 4.5). The increases in JJA linked to the degradation in the NH high latitudes are particularly prominent. The net effect of this is an increase in SST RMSE by approximately 1%.

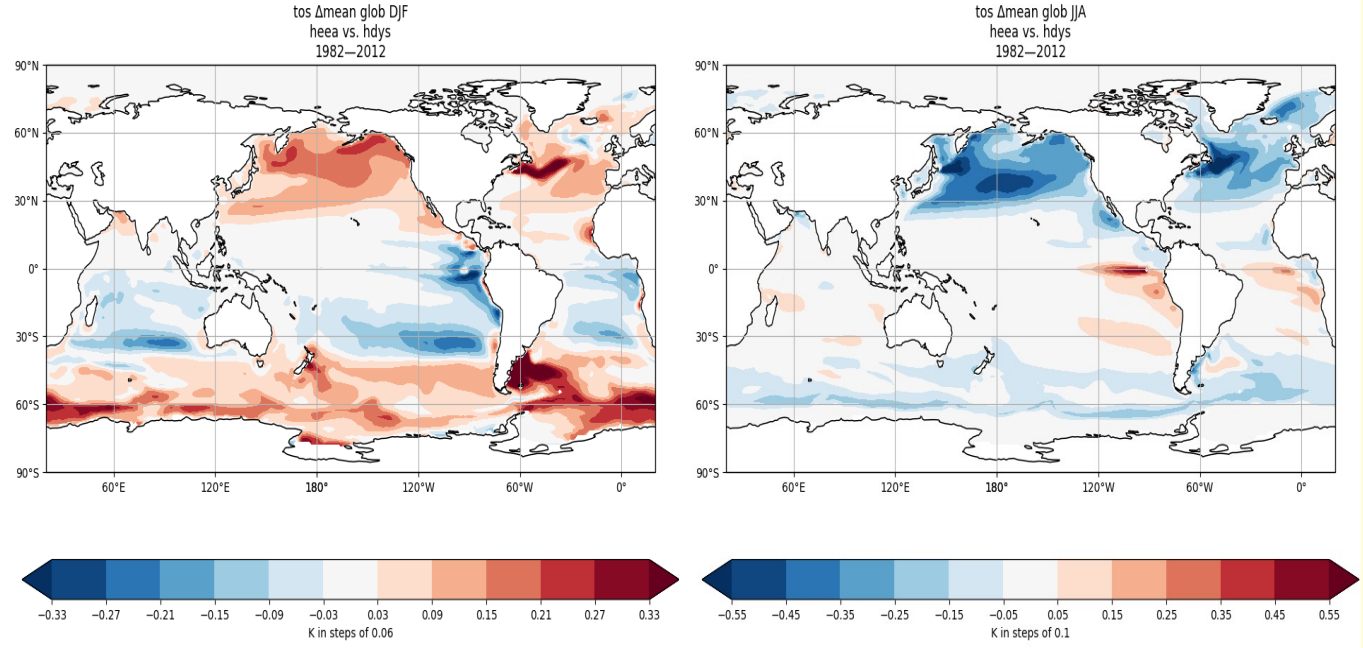

Figure 4.3. Mean difference in sea-surface temperature between the WO_MIXING and CONTROL simulations for the months DJF (left) and JJA (right) for the years 1982-2012.

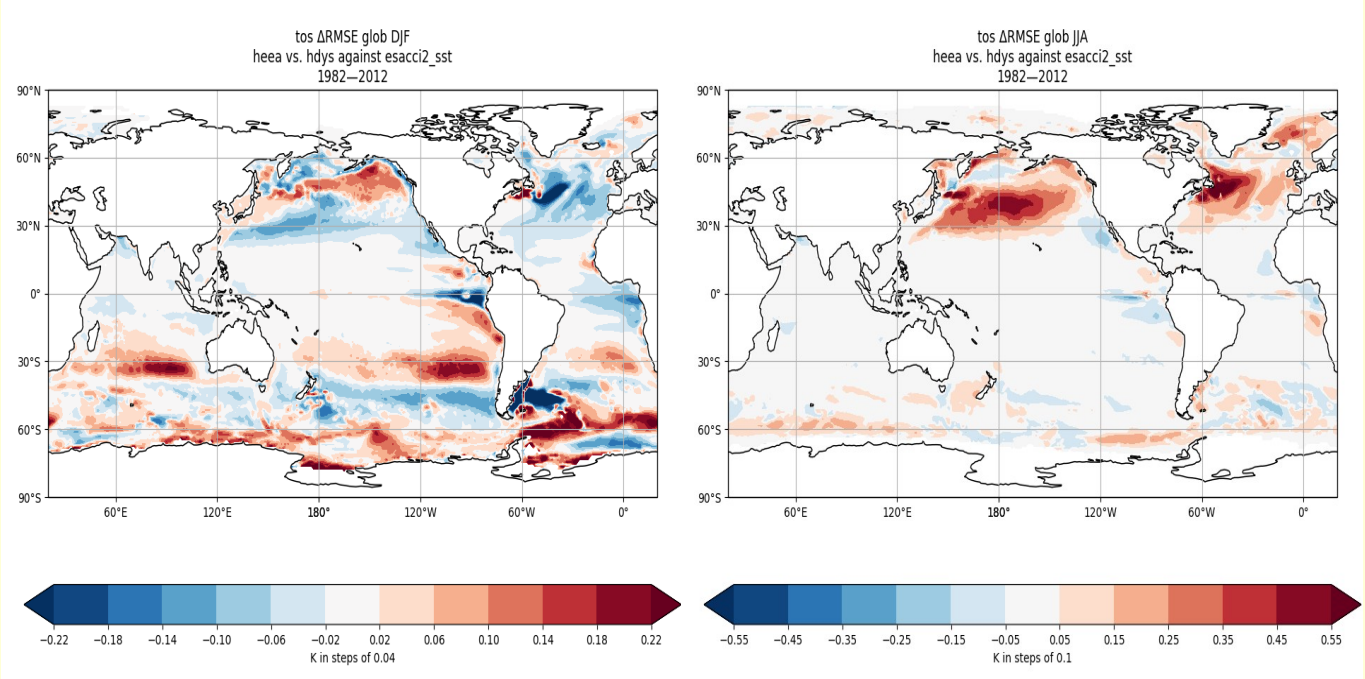

Figure 4.4. Mean difference in sea-surface temperature RMSE between the WO_MIXING and CONTROL simulations for the months DJF (left) and JJA (right) for the years 1982-2012.

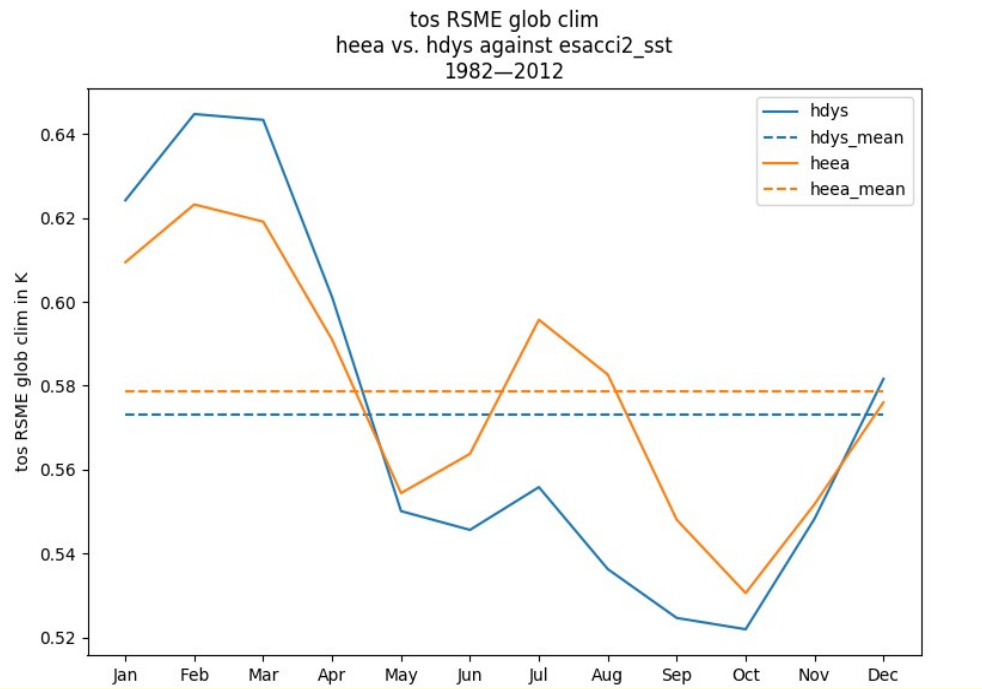

Figure 4.5. Sea-surface temperature RMSE climatology for the WO_MIXING and CONTROL simulations for the years 1982-2012.

The effects of these changes in mixing are not limited to temperature at the ocean surface, but extend throughout much of the upper ocean. The widespread warming noted previously for the surface in DJF (across the mid- and high- latitudes) actually extends down through much of the upper ocean (0-200m; Fig. 4.6). The magnitude of this is largest in the SH mid-latitudes. We also see another interesting effect here: a reciprocal cooling below concentrated between the depths of 75-150m around ~30°S. This region of cooling expands to the full 0-200m range in JJA, albeit with a slightly decreased magnitude. For JJA we also see a cooling signal at the surface (0-25m) sitting atop the warming signal in the NH mid- to high- latitudes. This acts to reduce biases throughout almost all regions of the upper ocean, but particularly for the NH mid-latitudes (RMSE decreases of up to 0.11K; Fig. 4.7). The exception to this is the SH high-latitudes where we see an increase in RMSE throughout the column. With respect to total-ocean means, we see a year-round decrease for RMSE of θ in the WO_MIXING simulation (Fig. 4.8). This θ decrease in RMSE is approximately 1%.

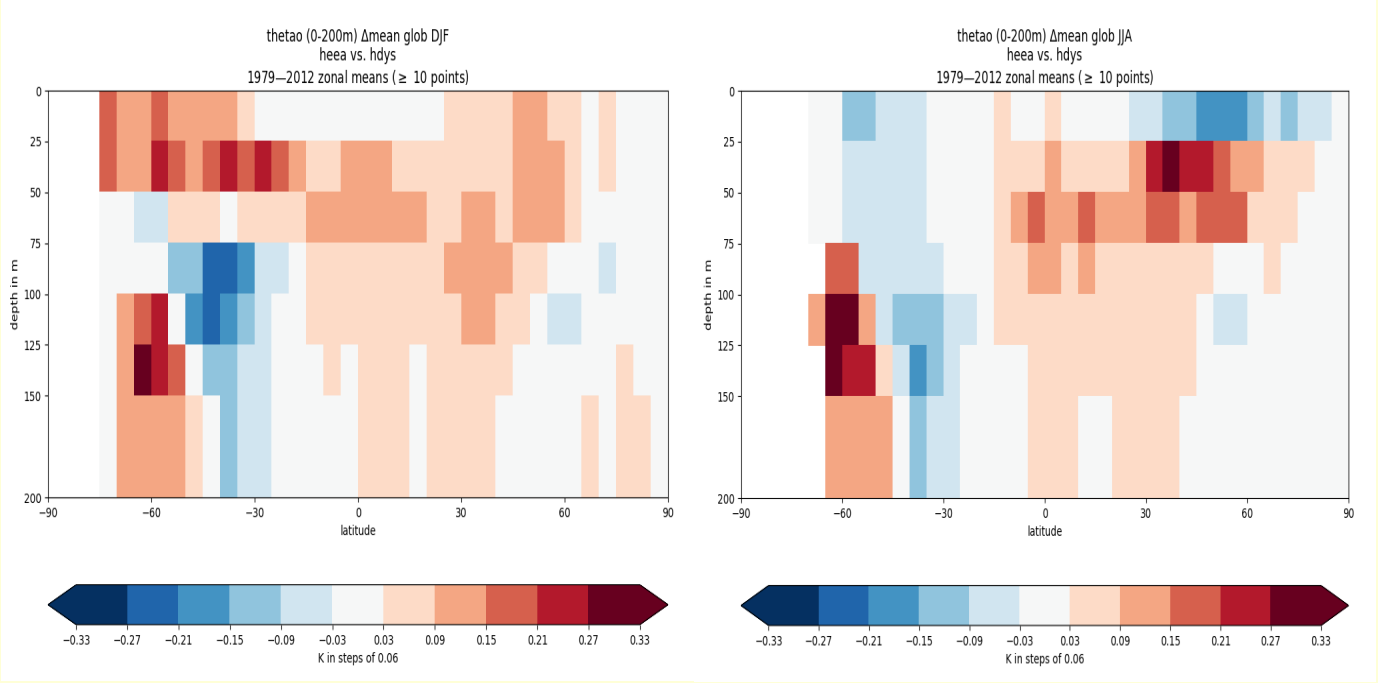

Figure 4.6. Mean difference in potential temperature between the WO_MIXING and CONTROL simulations for the months DJF (left) and JJA (right) for the years 1982-2012.

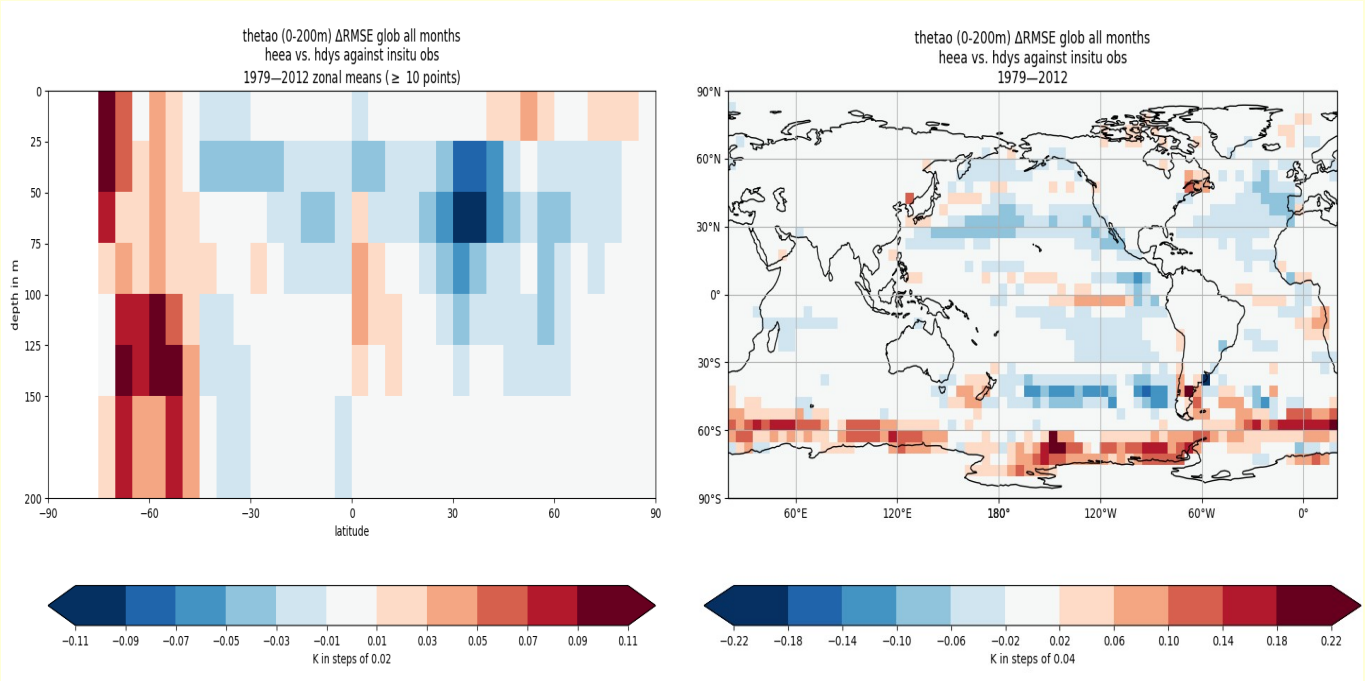

Figure 4.7. Mean difference in potential temperature RMSE between the WO_MIXING and CONTROL simulations for the years 1979-2012. **LEFT:** zonal average; **RIGHT:** vertical average (upper 200m).

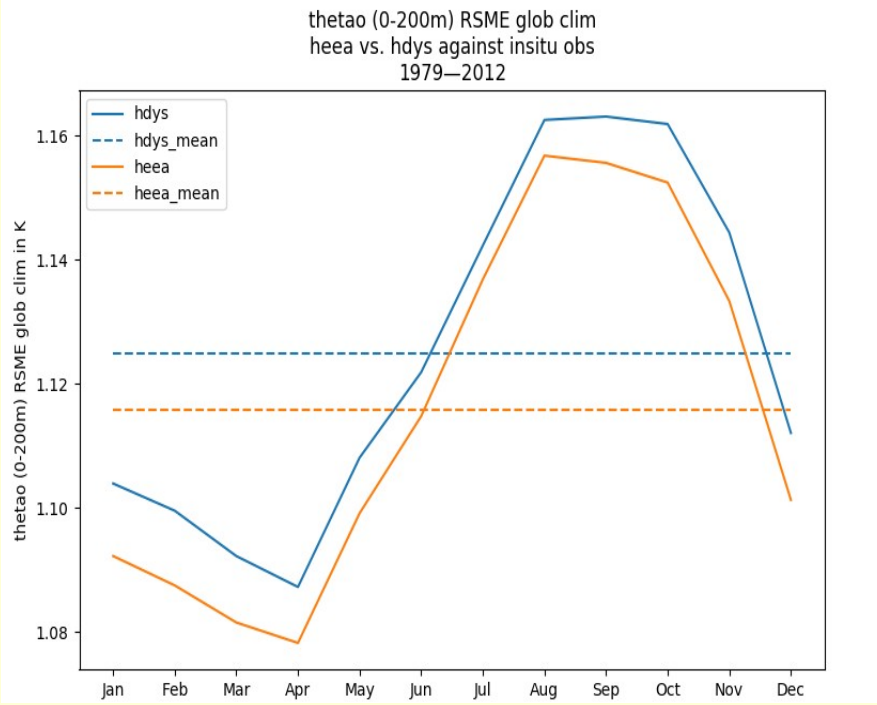

Figure 4.8. Potential temperature (upper 200m) RMSE climatology for the WO_MIXING and CONTROL simulations for the years 1979-2012.

4.4. Discussion

Here we have implemented a representation of wave orbital-induced turbulence into NEMO with the aim of rectifying NEMO's bias in mixed layer depth in a physical manner. This is done using the parameterisation of GB14. The first iteration of this was unsatisfactory, with the parameterisation producing too much mixing. As such, we explored various methods of correcting this. We were able to achieve realistic results via a reduction in the b_1 value from $b_1=1.4*10^{-3}$ to $b_1=0.7*10^{-4}$ (reduced to 5% of its original value; Equation 4.5). This original value of $b_1=1.4*10^{-3}$ comes from a study on swell attenuation (i.e. the energy lost from the waves) by Young et al. (2013). By using this value in the GB14 parameterisation we are making two assumptions: 1) all swell energy lost is converted to TKE with 100% conversion efficiency, and 2) this TKE is deposited only within the ocean. With regards to assumption 1, in reality is unlikely to achieve anywhere near 100% conversion efficiency. With regards to assumption 2, we note that it is also likely that some of this TKE goes into the atmosphere. Ardhuin et al. (2009) outlines a similar for model for swell attenuation whereby the atmosphere is the dominant sink for this energy. For a more robust implementation of the GB14 parameterisation, we require it to be modified in the following way

$$P_{\text{wom}}(z)=b_1 b_2 b_3 k\left(\frac{\omega_p H_S}{2} e^{-kz}\right)^3 \quad , \quad 0<\{b_2,b_3\}<1 \qquad (4.6)$$

where b_2 and b_3 are the new coefficients designed to deal with the two implicit assumptions in the GB14 parameterisation. b_2 is the proportion of swell-related energy that actually goes into the ocean (as opposed to the atmosphere) and b_3 is the proportion of this energy that is converted to TKE. With these two additional considerations, the aforementioned reduction in b_1 required to achieve realistic results seems appropriate. These two additional parameters are flagged here as an area for future research.

We also explored a wave-steepness dependent form of the GB14 parameterisation to alter the geographical distribution and seasonality of the mixing in a physically meaningful way, where b_1 is replaced by a reduced version of itself in the form of $b_{1\,\text{reduc}}$

$$b_{1\,\text{reduc}} = F^{\beta-1}\left(\frac{H_S k_p}{2}\right)^{\beta} b_1 \qquad (4.7)$$

where F is a normalisation factor and β is an integer. Values of between 0 and 5 were tested for β and 16 and 25 for F. This was unable to improve the current model biases but could be useful in the future as the model and its biases evolve.

Here I would also like to outline a way in which the representation of wave-orbital induced turbulence could be improved in the near future. The parameterisation of GB14 assumes monochromatic waves. This is a good assumption for a simple sea state with one peak in the wave energy spectrum, but becomes an issue if we consider a more complex sea-state with multiple peaks (the more typical case in the ocean). This swell attenuation and swell-related turbulence production would therefore be most accurate if computed for individual wave components rather than for peak wave parameters. This is done explicitly for swell dissipation within our wave models. Within the wave model, this could then be simply converted to the associated turbulence flux by integrating across all wave frequencies.

$$\phi_{\text{wom spectral}} = \rho g \left(\int_0^{f_c} S_{\text{swldiss}}\, df + \int_{f_c}^{\infty} S_{\text{swldiss}}\, df \right) \qquad (4.8)$$

where f_c is the high-frequency cut-off point which the wave model does not resolve. As this is largely a swell-related process, it mainly acts on lower frequencies and we can assume that the magnitude of this attenuation is negligible for the high frequencies.

$$\int_{f_c}^{\infty} S_{\text{swldiss}}\, df \simeq 0 \qquad (4.9)$$

$$\phi_{\text{wom}} = \rho g \left(\int_0^{f_c} S_{\text{swldiss}}\, df + \int_{f_c}^{\infty} S_{\text{swldiss}}\, df \right) \qquad (4.10)$$

$$\simeq \rho g \int_0^{f_c} S_{\text{swldiss}}\, df \qquad (4.11)$$

This could then be additional diagnostic output from the wave model used for coupling to the ocean. In regards to the depth deposition of this energy, we can follow the same method as GB14, which is based upon earlier work by Babanin (2006) which models the depth deposition of the wave-orbital induced turbulence as $e^{-3k_p z}$, where k_p is the peak wavenumber.

$$P_{\mathrm{wom}}(z) = 3k_p \phi_{\mathrm{wom}} e^{-3k_p z} \qquad (4.12)$$

This, however, still relies on peak wave number. We could be yet more consistent if we pass the spectral term S_{swldiss} out of the wave model and use this to find a spectral version of ϕ_{wom} which we could deposit the turbulent energy from each frequency bin with the relevant depth-deposition profile.

With regards to wave-breaking related turbulence, we have used the flux-based representation of Breivik et al. (2014) which assumes that all wave-breaking related turbulence is injected into the surface, neglecting any depth-based representation of the turbulence. This is justifiable on the basis that the strongest wave breaking-related turbulence is restrained to depths of the order of wave height (order 1m), with the turbulence below this depth diffusing rapidly (Thomson et al., 2016). The vertical resolution at the surface of the NEMO version in which this was implemented (NEMO3.4) was approximately 10m and therefore injection into the surface layer was appropriate. The version of NEMO used in this study (NEMO4.01) has a much higher resolution at the surface (1m), meaning that a representation of wave breaking which explicitly considers the vertical depth penetration of this turbulence warranted investigation. Janssen (2012) proposes a suitable alternative method of representing the effect of turbulence by wave breaking. Instead of representing this turbulent energy as a surface flux and allowing its vertical transport advection of this turbulence to be handled solely by the TKE scheme, Janssen (2012) explicitly models the depth deposition of the wave breaking related TKE using a profile that decays exponentially with depth. This parameterisation had previously been implemented within NEMO3.4, but could not offer model improvement at the time and was therefore not taken further. With the hypothesis that the limitation here was insufficient vertical resolution, we re-implemented Janssen's (2012) model for turbulence due to wave breaking in NEMO4.01. After some experimentation with the vertical depth penetration scale of the Janssen (2012) model, we found that it was unable to offer any improvements over the Breivik et al. (2014) flux-based representation with respect to model biases, and we therefore continued with the Breivik et al. (2014) model.

4.5. Concluding remarks

This chapter documents the introduction of wave-orbital induced turbulence into NEMO. We run a 33-year hindcast with our new model (WO_MIXING) and compare it to the operational standard (CONTROL). The CONTROL simulation contains an *ad hoc* empirical solution to the too-shallow mixed layer bias in NEMO. This empirical function is turned off in WO_MIXING. Relative to the CONTROL, we find that the WO_MIXING simulation has a deeper mixed layer generally, except for in SH winter in which we see a considerable shallowing of the Southern Ocean mixed layer. WO_MIXING is more accurate with respect to Argo observations of climatological mixed layer. These changes in mixing leads to a warming (cooling) of SST in the high-latitudes and a cooling (warming) for the mid-latitudes for DJF (JJA) in WO_MIXING. This degrades performance of SST with respect to the ESACCI satellites, particularly in the North Pacific. WO_MIXING is also generally warmer throughout the upper 200m of the ocean. This reduces temperature biases in all areas except the SH high-latitudes, leading to a net improvement in performance of about 1%. These findings suggest that the too-shallow mixed layer bias in NEMO may be due to the neglect of wave-orbital induced turbulence, and that the inclusion of this phenomenon can replace the *ad hoc* empirical solution currently employed within NEMO. The next step is to test with the latest version of NEMO4.0 planned for CY49R1, and then fully coupled to the atmosphere and waves.

Although the ocean, waves, sea ice and the atmosphere are heavily intertwined, too often modellers from one discipline will ignore their adjacent counterparts. This chapter contributes to the overall aim of this thesis to improve interoperability of these models whilst staying true to the physics that governs these interactions.

4.6. References

Aksenov, Y., Blockley, E., Chevallier, M., Feltham, D. L., Fichefet, T., Garric, G., Holland, P., Iovino, D., Madec, G., Massonnet, F., Ridley, J., Rousset, C., Salas, D., Schroeder, D., Tietsche, S., & Vancoppenolle, M. (2019). Sea Ice modelling Integrated Initiative (SI^3) -- The NEMO Sea Ice engine. In *ISSN 1288-1619, Institut Pierre-Simon Laplace (IPSL)* (Issue 31). https://doi.org/10.5281/zenodo.1471689

Babanin, A. V. (2006). On a wave-induced turbulence and a wave-mixed upper ocean layer. *Geophysical Research Letters*, *33*(L20605). https://doi.org/10.1029/2006GL027308

Babanin, A. V. (2009). Breaking and dissipation of Ocean surface waves. In *Breaking and Dissipation of Ocean Surface Waves* (Issue January 2009). https://doi.org/10.1017/CBO9780511736162

Babanin, A. V., & Chalikov, D. (2012). Numerical investigation of turbulence generation in non-breaking potential waves. *Journal of Geophysical Research: Oceans*, *117*(6), 1–14. https://doi.org/10.1029/2012JC007929

Babanin, A. V., & Haus, B. K. (2009). On the Existence of Water Turbulence Induced by Nonbreaking Surface Waves. *Journal of Physical Oceanography*, *39*(10), 2675–2679. https://doi.org/10.1175/2009JPO4202.1

Benilov, A. Y. (2012). On the turbulence generated by the potential surface waves. *Journal of Geophysical Research: Oceans*, *117*(C00J30). https://doi.org/10.1029/2012JC007948

Bowden, K. F. (1950). The effect of eddy viscosity on ocean waves. *Philosophy Magazine*, *41*, 907–917.

Breivik, Ø., Mogensen, K., Bidlot, J.-R., Balmaseda, A., & Janssen, P. A. E. M. (2014). Surface wave effects in the NEMO ocean model: Forced and coupled experiments. *Journal of Geophysical Research: Oceans*, *120*, 2973–2992. https://doi.org/10.1002/2014JC010565.Received

Cavaleri, L., Fox-Kemper, B., & Hemer, M. A. (2012). Wind waves in the coupled climate system. *Bulletin of the American Meteorological Society*, *93*(11), 1651–1661. https://doi.org/10.1175/BAMS-D-11-00170.1

Ghantous, M., & Babanin, A. V. (2014). One-dimensional modelling of upper ocean mixing by turbulence due to wave orbital motion. *Nonlinear Processes in Geophysics*, *21*(1), 325–338. https://doi.org/10.5194/npg-21-325-2014

Hersbach, H., Bell, B., Berrisford, P., Hirahara, S., Horányi, A., Muñoz-Sabater, J., Nicolas, J., Peubey, C., Radu, R., Schepers, D., Simmons, A., Soci, C., Abdalla, S., Abellan, X., Balsamo, G., Bechtold, P., Biavati, G., Bidlot, J., Bonavita, M., … Thépaut, J. N. (2020). The ERA5 global reanalysis. *Quarterly Journal of the Royal Meteorological Society*, *146*(730), 1999–2049. https://doi.org/10.1002/qj.3803

Huang, C. J., Qiao, F., Shu, Q., & Song, Z. (2012). Evaluating austral summer mixed-layer response to surface wave-induced mixing in the Southern Ocean. *Journal of Geophysical Research: Oceans*, *117*(6), 1–10. https://doi.org/10.1029/2012JC007892

Janssen, P. A. E. M. (2004). *The interaction of ocean waves and wind*. Cambridge University Press.

Janssen, P. A. E. M. (2012). Ocean wave effects on the daily cycle in SST. *Journal of Geophysical Research: Oceans*, *117*(9). https://doi.org/10.1029/2012JC007943

Kolmogorov, A. N. (1942). Equations of turbulent motion in an incompressible fluid. *Izvestiya Akademiya Nauk SSSR*, *6*, 56–58.

Kukulka, T., & Brunner, K. (2015). Passuve Buoyant Tracers in the Ocean Surface Boundary Layer: 1. Influence of Equilibrium Wind-Waves on Vertical Distributions. *Journal of Geophysical Research: Oceans*, *120*, 4324–4339. https://doi.org/10.1002/2015JC011301

Madec, & The NEMO Team, A. (2019). NEMO ocean engine. *Scientific Notes of Climate Modelling Center (27)*, ISSN 1288-1619, Institut Pierre-Simon Laplace. https://doi.org/10.5281/zenodo.1464816

McWilliams, J. C., Sullivan, P. P., & Moeng, C. H. (1997). Langmuir turbulence in the ocean. *Journal of Fluid Mechanics*, *334*, 1–30. https://doi.org/10.1017/S0022112096004375

Pleskachevsky, A., Dobrynin, M., Babanin, A. V., Günther, H., & Stanev, E. (2011). Turbulent Mixing due to Surface Waves Indicated by Remote Sensing of Suspended Particulate Matter and Its Implementation into Coupled Modeling of Waves, Turbulence, and Circulation. *Journal of Physical Oceanography*, *41*(4), 708–724. https://doi.org/10.1175/2010JPO4328.1

Qiao, F., Yuan, Y., Yang, Y., Zheng, Q., Xia, C., & Ma, J. (2004). Wave-induced mixing in the upper ocean: Distribution and application to a global ocean circulation model. *Geophysical Research Letters*, *31*(L11303). https://doi.org/10.1029/2004GL019824

Rodgers, K. B., Aumont, E., Mikaloff Fletcher, S. E., Plancherel, Y., Bopp, L., de Boyer Montégut, C., Iudicone, D., Keeling, R. F., Madec, G., & Wanninkhof, R. (2014). Strong sensitivity of southern ocean carbon uptake and nutrient cycling to wind stirring. *Biogeosciences*, *11*(15), 4077–4098.

Shu, Q., Qiao, F., Song, Z., Xia, C., & Yang, Y. (2011). Improvement of MOM4 by including surface wave-induced vertical mixing. *Ocean Modelling*, *40*(1), 42–51.

Song, Z., Qiao, F., & Wang, C. Z. (2011). The correctness to the spuriously simulated semi-annual cycle of the sea surface temperature in the equatorial eastern Pacific. *Science China Earth Sciences*, *54*(3), 438–444. https://doi.org/10.1007/s11430-011-4176-3

Stoney, L., Walsh, K. J. E., Thomas, S., Spence, P., & Babanin, A. V. (2018). Changes in Ocean Heat Content Caused by Wave-Induced Mixing in a High-Resolution Ocean Model. *Journal of Physical Oceanography*, *48*, 1139–1150. https://doi.org/10.1175/JPO-D-17-0142.1

Thomas, S., Babanin, A. V., Walsh, K. J. E., Stoney, L., & Heil, P. (2019). Effect of wave-induced mixing on sea ice in a high-resolution ocean model. *Ocean Dynamics*, *69*(6), 737–746. https://doi.org/10.1007/s10236-019-01268-0

Thomson, J., Schwendeman, M. S., Zippel, S. F., Moghimi, S., Gemmrich, J., & Rogers, W. E. (2016). Wave-Breaking Turbulence in the Ocean Surface Layer. *Journal of Physical Oceanography*, *46*(6), 1857–1870. https://doi.org/10.1175/JPO-D-15-0130.1

Toffoli, A., McConochie, J., Ghantous, M., Loffredo, L., & Babanin, A. V. (2012). The effect of wave-induced turbulence on the ocean mixed layer during tropical cyclones: Field observations on the Australian North-West Shelf. *Journal of Geophysical Research: Oceans*, *117*(C00J24), 1–8. https://doi.org/10.1029/2011JC007780

Walsh, K. J. E., Govekar, P., Babanin, A. V., Ghantous, M., Spence, P., & Scoccimarro, E. (2017). The effect on simulated ocean climate of a parameterization of unbroken wave-induced mixing incorporated into the k-epsilon mixing scheme. *Journal of Advances in Modeling Earth Systems*, *9*, 1–24. https://doi.org/10.1002/2016MS000707

Young, I. R., Babanin, A. V., & Zieger, S. (2013). The Decay Rate of Ocean Swell Observed by Altimeter. *Journal of Physical Oceanography*, *43*(11), 2322–2333. https://doi.org/10.1175/JPO-D-13-083.1

This page intentionally left blank.

This page intentionally left blank.

Chapter 5:

Conclusions and future research

In the first research chapter (Ch. 2), the BYDBR observation-based physics is introduced into the WAM wave model. This is the modern wave physics package for third generation spectral models, developed by A. V. Babanin, I. R. Young, M. A. Donelan, M. L. Banner and W. E. Rogers. Its source functions were measured and therefore are not subject to tuning (within confidence limits of the measurements), therefore departing from the semi-empirical approach used by other wave source term packages. This observation-based physics was already available in two of the three dominant third-generation spectral wave models, WAVEWATCH-III and SWAN, but not yet WAM. This introduction (coding, testing and validation for both the ECMWF- and Hereon-managed versions of WAM) was a key outcome of this thesis, and has now enabled use of this modern wave physics package by the remaining third of the research and practical oceanographic community (see Preface for code availability). This in itself was an immense task, involving more than 500,000 lines of code.

We find considerable differences between the WAM with the new observation-based physics and WAM with the operational standard, particularly for boreal winter in which we see widespread reductions in the NH for significant wave height and mean wave period of up to 5%. In other regions, particularly the eastern Pacific and the Southern Ocean, we see increases of almost the same magnitude. Despite these differences, performance on the global scale with respect to *in situ* measurements is similar. This chapter has opened the gateway to a whole new area of research. These questions are summarised here, but the reader is strongly encouraged to refer back to Chapter 2.4 for details: 1) What are the underlying cause of the differences between the two wave packages? 2) How do the two wave packages differ for extreme waves? 3) What would the biases and performance of each of the two wave packages if we were actually able to properly sample the global ocean? 4) What will the BYDBR observation-based physics when we operate in the two-way

mode of WAM? With the BYDBR observation-based physics implementation into WAM, we now have the possibility to answer such questions.

In the second research chapter (Ch. 3) we extend the observation-based approach to a new and challenging region: the Marginal Ice Zone. This observation-based approach is used to form a physically-based new model to represent interactions between waves and sea ice. The model can be summarised as follows: 1) sea ice takes a binary form, either 'broken' or 'unbroken', 2) waves can break sea ice, transitioning it from unbroken to broken, 3) an observation-based non-dimensional threshold is used to identify when this occurs, 4) there are two modes of attenuation for waves in ice (dependent upon the ice state), representing the on/off attenuation reported in the literature, 5) through the attenuation and ice break-up described above, we achieve two-way wave-sea ice coupling, thereby allowing wave-sea ice feedbacks. We note here that this study is the first to implement observation-based features 3) and 4) within a numerical wave model.

Our new model for wave-sea ice interaction is then applied to a case study of the Davis Sea in the Antarctic. We find that the model is able to very accurately simulate both the waves within the Marginal Ice Zone, and the evolution of the Marginal Ice Zone itself, particularly with respect to break-up of the sea ice. Our model assumes that this break-up is based exclusively on waves (i.e. neglects the effects of winds or currents), and its faithfulness to reality substantiates the critical role that waves can play on the morphology of the Marginal Ice Zone. Next we will explore this model for wave-sea ice interaction on the global scale, i.e. including the entirety of the Arctic and Antarctic, from which we can test the globalism of the conclusions drawn from our case study, and discover more about the polar regions more generally.

In the third research chapter (Ch. 4) we bring the missing observation-based wave physics into the ocean. First, we add the missing wave-related physics into an ocean general circulation model. We find that the this effect, wave-orbital induced mixing, is of considerable impact within the ocean. We compare our implementation with the wave-related physics against the standard version of NEMO, which includes an *ad hoc* solution to the too-shallow mixed layer in NEMO. We find that our new wave physics setup deepens the mixed layer relative to the control, except for the considerable shallowing seen in the Southern Ocean in Austral winter. These changes in mixing brings the model closer to *in situ* observations of mixed layer depth. These changes in mixing have

a flow-on effect for heat fluxes, leading to a warming (cooling) of SST in the high-latitudes and a cooling (warming) for the mid-latitudes for DJF (JJA). This results in a slight increase in SST bias, most prominent in the high-latitudes of the North Pacific and North Atlantic for JJA. Considering deeper regions (to depths of 200m), we see a generally warmer ocean, which reduces biases in potential temperature. These results show that wave-orbital induced turbulence seems to fit the bill for the missing source of mixing in NEMO, the absence of which led to the *ad hoc* solution currently in place to counter this shallow bias in mixed layer.

This thesis contributes some key building blocks in moving towards a more physical representation and deeper understanding of waves and wave-coupled processes, but it is clear that there is much work to be done yet.

References

These are the references for chapter 1 and 5. References for the research chapters (Ch. 2-4) are found within.

Ardhuin, Fabrice, Erick Rogers, Alexander V. Babanin, Jean François Filipot, Rudy Magne, Aaron Roland, Andre van der Westhuysen, et al. 2010. “Semiempirical Dissipation Source Functions for Ocean Waves. Part I: Definition, Calibration, and Validation.” *Journal of Physical Oceanography* 40 (9): 1917–41. https://doi.org/10.1175/2010JPO4324.1.

Babanin, Alexander V. 2012. “Swell Attenuation Due to Wave-Induced Turbulence.” In *Proceedings of the ASME 2012 31st International Conference on Ocean, Offshore and Arctic Engineering OMAE2012, July 1-6, 2012, Rio de Janeiro, Brazil*, ISBN 978-0-7918-4489-2, 5p. https://doi.org/10.1115/OMAE2012-83706.

Babanin, Alexander V., M. L. Banner, Ian R. Young, and M. A. Donelan. 2007. “Wave Follower Measurements of the Wind Input Spectral Function. Part 3. Parameterization of the Wind Input Enhancement Due to Wave Breaking.” *Journal of Physical Oceanography* 37 (11): 2764–75. https://doi.org/10.1175/JPO3147.1.

Babanin, Alexander V., K. N. Tsagareli, Ian R. Young, and D. J. Walker. 2007. “Implementation of New Experimental Input/Dissipation Terms for Modeling Spectral Evolution of Wind Waves.” In *Proceedings of the 10th International Workshop on Wave Hindcasting and Forecasting and Coastal Hazards, Oahu, Hawaii, November, 11-16, 2007*, Sponsors: U.S. Army Engineer Research and Developm.

———. 2010. “Numerical Investigation of Spectral Evolution of Wind Waves. Part 2. Dissipation Function and Evolution Tests.” *Journal of Physical Oceanography* 40 (4): 667–83.

Babanin, Alexander V., and Ian R. Young. 2005. “Two-Phase Behaviour of the Spectral Dissipation of Wind Waves.” In *Proceedings Ocean Waves Measurement and Analysis, Fifth International Symposium WAVES2005, 3-7 July, 2005, Madrid, Spain*, Sponsors: CEDEX (Spain) and CORPI of ASCI (USA), p.

Babanin, Alexander V., Ian R. Young, M. A. Donelan, William Erick Rogers, Stefan Zieger, and Qingxiang Liu. 2019. “S_{in} + S_{ds} : Rogers et al. 2012 & Zieger et al. 2015.” In Section 2.3.11 of *The WAVEWATCH III® Development Group (WW3DG), (2019): User manual and system documentation of WAVEWATCH III® version 6.07. Tech. Note 333, NOAA/NWS/NCEP/MMAB, College Park, MD, USA, 465 pp. + Appendices.*

Donelan, M. A., Alexander V. Babanin, Ian R. Young, and M. L. Banner. 2006. “Wave Follower Measurements of the Wind Input Spectral Function. Part 2. Parameterization of the Wind Input.” *Journal of Physical Oceanography* 36 (8): 1672–88.

Liu, Qingxiang, W. Erick Rogers, Alexander V. Babanin, Ian R. Young, Leonel Romero, Stefan Zieger, Fangli Qiao, and Changlong Guan. 2019. “Observation-Based Source Terms in the Third-Generation Wave Model WAVEWATCH III: Updates and Verification.” *Journal of Physical Oceanography* 49 (2): 489–517. https://doi.org/10.1175/JPO-D-18-0137.1.

Tsagareli, K. N., A. V. Babanin, D. J. Walker, and I. R. Young. 2010. “Numerical Investigation of Spectral Evolution of Wind Waves. Part I: Wind-Input Source Function.” *Journal of Physical Oceanography* 40 (4): 656–66. https://doi.org/10.1175/2009JPO4345.1.

Young, Ian R., and Alexander V. Babanin. 2006. “Spectral Distribution of Energy Dissipation of Wind-Generated Waves Due to Dominant Wave Breaking.” *Journal of Physical Oceanography* 36 (3): 376–94.